ACTIVE FLOW CONTROL STUDIES OVER AN ELLIPTICAL PROFILE

A THESIS SUBMITTED TO
THE GRADUATE SCHOOL OF NATURAL AND APPLIED SCIENCES
OF
MIDDLE EAST TECHNICAL UNIVERSITY

BY

ENGİN ERLER

IN PARTIAL FULFILLMENT OF THE REQUIREMENTS
FOR
THE DEGREE OF MASTER OF SCIENCE
IN
AEROSPACE ENGINEERING

SEPTEMBER 2008

Approval of the thesis:

ACTIVE FLOW CONTROL STUDIES OVER AN ELLIPTICAL PROFILE

submitted by **ENGİN ERLER** in partial fulfillment of the requirements for the degree of **Master of Science in Aerospace Engineering Department, Middle East Technical University** by,

Prof. Dr. Canan Özgen
Dean, Gradute School of **Natural and Applied Sciences** _____

Prof. Dr. İsmail H. Tuncer
Head of Department, **Aerospace Engineering** _____

Prof. Dr. İsmail H. Tuncer
Supervisor, **Aerospace Engineering Dept., METU** _____

Examining Committee Members:

Assoc. Prof. Dr. Serkan Özgen
Aerospace Engineering Dept., METU _____

Prof. Dr. İsmail H. Tuncer
Aerospace Engineering Dept., METU _____

Assist. Prof. Dr. Nilay Sezer Uzol
Mechanical Engineering Dept., TOBB ETU _____

Dr. D. Funda Kurtuluş
Aerospace Engineering Dept., METU _____

Dr. Özgür Uğraş Baran
Senior System Engineer, HAVELSAN _____

Date: _____

I hereby declare that all information in this document has been obtained and presented in accordance with academic rules and ethical conduct. I also declare that, as required by these rules and conduct, I have fully cited and referenced all material and results that are not original to this work.

Name, Last Name: Engin Erler

Signature :

ABSTRACT

ACTIVE FLOW CONTROL STUDIES OVER AN ELLIPTICAL PROFILE

Erler, Engin
M.S., Department of Aerospace Engineering
Supervisor : Prof. Dr. İsmail H. Tuncer

September 2008, 66 pages

Active flow control by a jet over a 12.5% thick elliptic profile is investigated numerically. Unsteady flowfields are calculated with a Navier Stokes solver. The numerical method is first validated without the jet and with the presence of steady-blowing and pulsating jets. Three jet types, namely steady, pulsating and synthetic jets, are next compared with each other and it is shown that the most drag reduction is achieved by a synthetic jet and the most lift enhancement is achieved by a steady jet. The influences of the jet location, the jet velocity, the jet frequency, the jet slot length and the jet angle on the flowfield is parametrically studied. It is shown that the jet location and the jet velocity are the most effective parameters. The jet parameters are optimized to minimize the drag coefficient while keeping the jet power constant. The drag is reduced by 32.5% for the angle of attack 0^o and by 24% for the angle of attack 4^o.

Keywords: Active Flow Control, Computational Fluid Dynamics, Elliptical Profile, Response Surface Methodology

ÖZ

BİR ELİPTİK PROFİL ÜZERİNDE AKTİF AKIŞ KONTROLÜ ÇALIŞMALARI

Erler, Engin

Yüksek Lisans, Havacılık ve Uzay Mühendisliği Bölümü

Tez Yöneticisi : Prof. Dr. İsmail H. Tuncer

Eylül 2008, 66 sayfa

Bir jet ile yapılan aktif akış kontrolü, %12.5 kalınlıktaki bir eliptik profil üzerinde sayısal yöntemlerle incelenmiştir. İlk olarak, sayısal yöntem jet olmadığında ve sürekli üfleyen ve periyodik üfleyen jetler olduğunda doğrulanmıştır. Daha sonra, üç jet çeşidi, yani sürekli üfleyen, periyodik üfleyen ve sentetik jet karşılaştırılmış ve sürükleme kuvvetini en çok sentetik jetin azalttığı ve kaldırma kuvvetini en çok sürekli üfleyen jetin arttırdığı gösterilmiştir. Jetin yeri, açısı, hızı, genişliği ve frekansının etkisi parametrik olarak incelenmiştir. Jetin yeri ve jetin hızının en etkili parametreler olduğu gösterilmiştir. Jet parametreleri en düşük sürükleme kuvveti için sabit güç koşullarında optimize edilmiştir. Sürükleme kuvveti, hücum açısı 0^o için %32.5, hücum açısı 4^o için %24 azaltılmıştır.

Anahtar Kelimeler: Aktif Akış Kontrolü, Hesaplamalı Akışkanlar Dinamiği, Eliptik Kanat Profili, Yanıt Yüzey Yöntemi

Dedicated to my beloved father

ACKNOWLEDGMENTS

In Aerospace Engineering Department, first, I want to thank my supervisor Prof. Dr. İsmail H. Tuncer for his assistance and advisories about my thesis. Also thanks to the jury members for their corrections and advices. I am grateful to Dr. Mustafa Kaya about his help on parallel computing and optimization.

In Havelsan, I am thankful to Dr. Özgür Uğraş Baran to answer my endless questions. Also, Gülsüm Hilal Erçin and Ethem Hakan Orhan for supporting me.

Also in my family, I want to thank my grandmother, grandfather, my mother for their support. I especially want to thank my sister for English corrections.

Lastly, I want to thank Eray Akçayöz for his friendship and support.

Also, I want to thank everybody that contributed to my thesis.

TABLE OF CONTENTS

LIST OF TABLES

TABLES

LIST OF FIGURES

FIGURES

LIST OF ABBREVIATIONS

ROMAN SYMBOLS

a	Speed of sound
c	Chord of the profile
C_d	Drag coefficient
C_l	Lift coefficient
C_μ	Jet momentum coefficient
C_p	Jet power coefficient
e	Energy
F	Frequency
F^+	Nondimensional jet frequency with freestream velocity
J	Jacobian
M	Mach number
p	Static pressure
Pr	Prandtl number
R	Gas constant
Re	Reynolds number
s	Entropy
t	Time
T	Temperature
u	Velocity component in ξ direction (Grid along direction)
w	Velocity component in η direction (Grid normal direction)
$\vec{\mathbf{V}}$	Velocity vector
x	Cartesian, spatial coordinate for streamwise direction
z	Cartesian, spatial coordinate for transverse direction

GREEK SYMBOLS

α	Angle of Attack
γ	Specific heat ratio
η	Curvilinear, spatial coordinate for grid normal direction
μ	Dynamic viscosity
ν	Kinematic viscosity
ρ	Density
Ω	Rotation vector
ξ	Curvilinear, spatial coordinate for grid along direction

SUBSCRIPTS

∞	Freestream values
jet	Jet values
t	Turbulent values

SUPERSCRIPTS

$*$	Dimensional

CHAPTER 1

INTRODUCTION

High thrust, high lift, low weight and low drag are the main requirements of the current aircraft. In recent years, the studies show that all these requirements can be met by active flow control. Active flow control is the ability of controlling the flow with addition of energy and without attachment of auxiliary devices such as riblets, flaps or large-eddy breakup devices [3]. Lift and thrust enhancement, drag reduction, noise abatement, stall delaying, full/partial flow reattachment, mixing enhancement are the main outcomes of active flow control. Altering the flow for maneuvering without using control surfaces gives the opportunity for low cost and low weight UAVs [4, 5]. Delaying stall with active flow control on the blades has shown to increase thrust for gas turbine engines [6]. For reducing the drag on the wings, active control of laminar-turbulent transition has been employed in many applications [7, 8, 9]. Investigations of development of high-lift systems are concentrated on application of active flow control for increasing the lift without changing the angle of attack or using flaps [10, 11, 12]. Helicopters can benefit from rapidly changing of lift and drag by using active flow control, for blade-vortex-interaction (BVI) noise reduction [13, 14].

One way of active flow control is blowing jets from the wing surfaces. Blowing jets are used in many applications for separation and circulation control. Steady and pulsed blowing have been used in many experimental and numerical applications to increase lift and/or decrease drag. The studies showed that blowing air only changes the resultant vector's direction, causing lift enhancement by compromising the drag reduction. However, application of these jets on real aircraft creates problems, such as the weight of special equipment to be carried and the increased energy requirement in the operation.

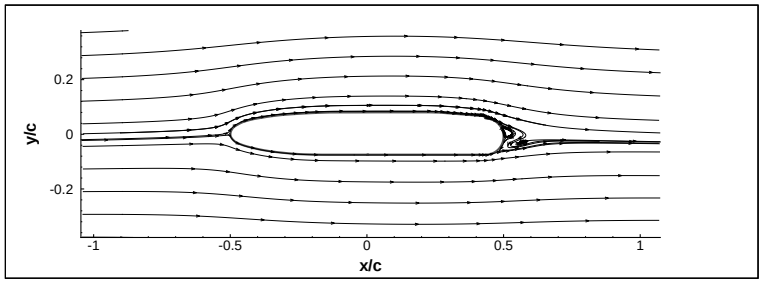

(a) Without jet

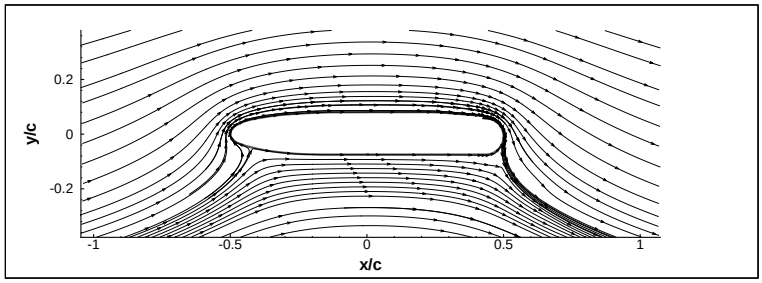

(b) With a Coanda jet

Figure 1.1: The Flow around an Elliptical Profile

Blowing jets are mostly used for circulation control of the blunt trailing edges. Blowing air near the trailing edge tangential to the surface, attaches the separated flow to the circular surface. This tendency of a stream of fluid to stay attached to a convex surface, rather than follow a straight line in its original direction is called *Coanda Effect*, and an example is shown in Figure 1.1. The principle was named after the Romanian researcher Henri Coanda, who was the first to understand the practical importance of the phenomenon for aircraft development. The Coanda effect is a result of the momentum of the gas and entrainment the air. As air flows over a convex airfoil, air is drawn down to adhere to the airfoil by a combination of the greater pressure above the gas flow and the lower pressure below the flow caused by an evacuating effect of the flow itself. As a result of shear flow, the slow-moving fluid trapped between the flow and the upper surface of the airfoil is rarefied [15].

Another way of active flow control is using synthetic jets, an example is presented in the Figure 1.2. The synthetic jet results from an oscillating membrane in an enclosed area with an orifice at the top. The oscillating membrane sucks the air from the orifice at the top, thus from the flow, and blows the air back into the flow. In this method, the flow gains momentum with introducing zero-net mass flux into the flow. Synthetic jets not only increase the lift, but also decrease the drag significantly. As opposed to blowing jets, synthetic jets do not

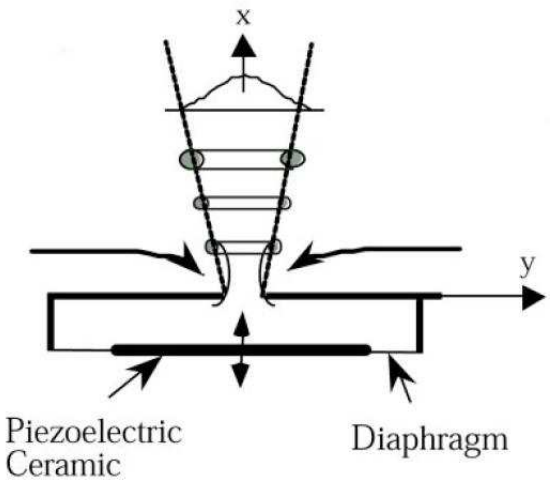

Figure 1.2: Synthetic Jet demonstration [1]

require special equipment or energy to blow the air. The oscillating membranes are activated using electrostatic or piezo-electric actuators and advancing technology gives the opportunity to create small and low cost jet actuators.

There are also other ways of active flow control like sucking jets, plasma jets, heaters, coolers, etc., which can change viscosity of flow, temperature of the flow or mass flux of the flow. However, in this thesis only blowing jets and synthetic jets are analyzed.

1.1 Experimental Studies

Flow control is discovered by Prandtl simultaneously with boundary layer theory a century ago [16]. During the Second World War, as well as the Cold War military needs have accelerated the flow control era [17, 18, 19]. After 1970, energy conservation and drag reduction has been widely researched for civilian air, sea and land vehicles. Large eddy breakup devices and riblets are developed to reduce the skin-friction drag in the turbulent layers [20, 21, 22, 23].

The first attempts to employ jets were with steady blowing jets. Henri Coanda investigated steady blowing jets over elliptical surfaces and invented the ”Coanda Jet” [15]. The Coanda effect is then studied for elliptical wings by tangential blowing near the trailing edge. The experimental and numerical studies have shown tremendous increase of lift with drag penalty (increase) [2, 24]. This phenomenon assisted the development of NOTAR concept in he-

licopters, in which a big jet using the flow of the engine is blown at the tail boom and it produces the thrust needed for anti-torque [25].

The next attempts to employ jets were with pulsed blowing jets. Seifert et al. [26] has worked experimentally on steady and oscillatory tangential blowing for several airfoils, namely NACA 0015, Eppler E-24 and PR8-40. To blow air, they have used two slots, which are at the leading edge of the airfoil and at the leading edge of the flap. They have investigated the effect of several parameters, namely the momentum coefficient of steady and oscillatory components of the blowing jet, the frequency of the oscillations, the shape and the incidence of the used airfoil. For NACA 0015 airfoil, it has been shown that steady blowing from leading edge with a jet momentum coefficient ($C_\mu = \frac{\rho_{jet} u_{jet}^{*2} w_{jet}^{*}}{\rho_\infty u_\infty^2 c}$) of 0.10 causes increase in lift and decrease in drag, but also causes decrease in the stall angle from 12 degrees to 8 degrees. On the other hand, oscillatory blowing with a jet momentum coefficient of 0.008 (C_μ=0.008) from the leading edge with a non-dimensional frequency ($F^+ = \frac{F_{jet}^{*}}{u_\infty / c}$) of 2, causes increase of lift coefficient (C_l), decrease of drag coefficient(C_d) and also increase of stall angle and maximum lift coefficient ($C_{l,max}$). Another result is, oscillatory blowing not only increases stall angle, but also decreases the momentum needed for higher C_l. For steady blowing, increasing C_μ causes increase of C_l, however, for oscillatory blowing increasing C_μ increases C_l to a peak then its effect decreases. The most effective F^+ has been found as 1. They have concluded that there were a lot of parameters to be investigated, so numerical tools would be useful.

The weight and energy constraints of blowing jets are currently overcome by the new type of jets, synthetic jets. Advancing technology gives opportunity to produce low cost and small synthetic jet actuators. Glezer and Amitay [1] have reviewed the previous studies on the synthetic jets. They have experimentally studied several jet parameters over a cylinder. The jet angle study shows that for angles less than 90 degrees applying jet increased lift and decreased drag, and between 90 and 130 degrees the lift and the drag decreased. However, more than 130 degrees of jet angle applying jet has a bad influence on the aerodynamic forces. The jet frequency study shows that the most effective jet frequency is at the order of 1 (F^+=1), however, if the actuation frequency is high enough ($F^+ > 2$), aerodynamic forces decouples from the jet frequency.

The location of the jet is one of the main important parameters being investigated. Locating the jet tangentially near the trailing edge is used for high-lift and circulation control, whereas,

locating the jet tangentially near the leading edge is used for separation control. Naini et al [27] have conducted an experimental study on excitation from tangential slots using piezoelectric actuators to control the flow over a circular cylinder. Jet location, amplitude and frequency are all quantified. The most effective parameter has been found as the jet location. They have shown that periodic excitation in front of the stagnation point helps bypassing the transition, modifying the shear layer and delaying the separation. In this study, the best frequency has been found as the natural shedding frequency which corresponds to non-dimensional jet frequency of 1 ($F^+ = 1$). Another observation is that by using front stagnation point and $F^+ = 1$, increasing the amplitude of the excitation increases the lift without changing the drag.

Siegel et al. [28] have also conducted an experimental study on the wake control of a circular cylinder and have designed a jet actuation system. The blowing jets are injected normal to the flow, from the upper side and the lower side. Open-loop control and close-loop control are investigated. In open-loop control, by blowing and sucking from different places, mass is introduced to the flow since blown and sucked gases are not equal. In closed-loop control, by blowing and sucking from different places at equal mass, mass is not introduced to the flow. This study has shown that the closed loop feedback reduces the drag and reduces the unsteadiness in the lift, but does not stabilize the wake. However, the open loop control stabilizes the wake, reduces the drag and reduces the unsteadiness in the lift. When the jet actuation system is located at the start location of the wake, the drag is further reduced by 90%.

Jones et al [29] have experimentally studied the circulation control with blowing jets around round trailing edge flapped airfoils, to reduce the side effects of high lifting devices like drag and mass flow. It is shown that locating the blowing jet at the upper side of the trailing edge of airfoil creates more lift than locating the blowing jet at the lower side of the trailing edge of airfoil. Another result observed is locating the blowing jets both at the upper side and the lower side of trailing edge causes reduction of the drag about 60%. Steady and pulsed blowing are compared by mass flow used and the results show that the pulsed blowing decreases mass flow needed by 50% for the same lift coefficient, and decreases the mass flow needed by 55-60% for the same lift to drag ratio.

Vismanath and Madhavan [30] have worked experimentally on steady tangential blowing from the trailing edge. They have tested a novel approach by putting the blowing slot down-

stream of the separation point. It is found that blowing inside the separation region, removes shear layer closure as opposed to blowing before separation bubble which is adopted by classical boundary layer theory. As the blowing slot approaches the separation point, much more separation control is obtained and the lift is increased as a result of Kutta condition.

1.2 Numerical Studies

A precise analysis of jets is limited due to its complexity. However, there have been a number of researchers who provided some progress on the simplification of the analysis. The common approach is to model the jet by changing the velocity wall boundary condition at the jet location. The effect of the oscillating diaphragm of synthetic jet and the effect of the pulsed blowing jets are simulated by a sinusoidal variation of the velocity.

Donovan et al. [31] have investigated the effect of steady jets and synthetic jets over NACA 0012 and NACA 0015. The profile of the jet is studied, and it is concluded that sin^2 profile best agrees with experiments and shows good numerical stability, however with constant jet momentum, all profiles exhibit similar results. It is shown that using steady or synthetic jet has negligible effects before separation. However, after separation starts, applying steady jet near the leading edge results in drag reduction even at low jet momentum coefficients by rotating the lift vector. Applying synthetic jet to NACA 0012 near the leading edge causes significant increase in the lift at about 29%.

Sankar et al. [32] have conducted a numerical study on steady and pulsed jets over a circulation control wing. Jet moment coefficients (C_μ) and jet frequencies in the range of 0-0.14 and 0-400 Hz are tested, respectively. For the same moment coefficient, the steady jet increases C_l more than the pulsed jet. For the same mass flow rate, 400 Hz pulsed jet has increased C_l more than steady jet. However, steady jet has increased C_l more than 40 Hz pulsed jet at the same mass flow rate. Moreover, steady jet has nearly same effect on the C_l with 120 Hz pulsed jet using the same mass flow rate. The best $C_l/(C_d+C_\mu)$ is achieved by steady jet, for the same moment coefficient and same mass flow rate. It is concluded that, as the jet frequency increases, the pulsed jet effect approaches to the steady jet effect.

Subhashni et al. [33] have studied the effect of injection and suction over a yawed cylinder numerically. It is demonstrated that multiple slot suction or moving slots downstream has

greater influence on flow as compared to the single slot suction with experimental validation. However, multiple slot injection has shown a reverse effect. Another result achieved is increasing the velocity of jet moves the separation point to the upstream.

Viken et al.[34] have conducted a research of effectiveness of different CFD codes on active flow control. This study compares experimental results of a hump model with three RANS solvers, which consisted of 2D unstructured, 3D unstructured and 3D structured codes using the thin layer boundary theory. Steady blowing, suction and oscillatory actuation have been tested. It is concluded that all CFD codes have discrepancies and the most significant discrepancies have been observed in the oscillatory action. The reasons are suggested as the insufficient modeling of turbulence and the insufficient identification of wall boundary conditions. To improve the solutions, using different turbulent models or DNS is recommended and remodeling of oscillatory movement is discussed.

1.3 The Objective of the Thesis

It is observed that active flow control can be employed for lift and thrust enhancement, drag reduction, noise abatement, stall delaying, separation control, full/partial flow reattachment, mixing enhancement. Many experimental and numerical studies are conducted on lift enhancement and drag reduction on wings. The lift enhancement is achieved by the circulation control for circular/elliptical trailing edge profiles; the drag reduction is achieved by the boundary layer control of the sharp edge profiles. However, very few investigations have studied the drag reduction on circular/elliptical trailing edge profiles with active flow control. Another observation is that in recent years, synthetic jet is gaining acceptance as it is smaller and it needs less power. Many studies are conducted on investigating the effects of synthetic jets for circular cylinders, airfoils and hump models. However, very few investigations have been studied for elliptical trailing edge profiles. Generally, steady jets are employed for elliptical trailing edge profiles.

The first objective of this thesis is to investigate the effects of active flow control over a 12.5% thick elliptic profile by using steady, pulsating and synthetic jets, numerically. The second objective of this thesis is to optimize jet parameters to minimize the drag of the 12.5% thick elliptic profile using synthetic jets. A compressible RANS solver is employed for unsteady flow

computations in parallel. The effects of steady-blowing, pulsating jet are validated against the experimental and numerical studies from literature. Three jet types, namely steady, pulsating and synthetic jets, are next compared with each other. The influence of jet parameters, namely the jet location, jet velocity, jet angle, jet frequency and jet slot width, are investigated parametrically. The jet parameters are finally optimized for minimizing the drag at various angles of attack. For decreasing computational time of optimization, an approximate method, Response Surface Method (RSM), is employed.

In Chapter 2, the formulation of the flow solver and parallel computation of the flow is given. The formulation of flow solver includes RANS equations and the effect of jet application to boundary conditions.

In Chapter 3, the optimization algorithm (RSM equations) is presented. Design of Experiment methods are discussed.

In Chapter 4, the results of validation of active flow control, preliminary studies and optimization of the jet parameters are demonstrated and the presented results are discussed according to previous studies from literature.

In Chapter 5, the concluding remarks and future studies are indicated.

CHAPTER 2

FLOW SOLUTION METHOD

2.1 Introduction

In this chapter, the flow solution methods employed to compute the unsteady viscous flowfields around the elliptical profiles are described. Unsteady flows are computed solving the Reynolds Averaged Navier Stokes solver over structured, body fitted grids. Spalart Allmaras turbulence model is employed for turbulence modeling. Computations are done in parallel, based on domain decomposition. PVM libraries are used in parallel solution algorithm. The computed flowfields are analyzed in terms of aerodynamic loads, averaged distribution of pressure and flow variables.

2.2 Navier-Stokes Solver

The finite difference formulation of Reynolds averaged Navier Stokes is solved in a computational domain discretized over a structured, body fitted grid. The non-dimensional form of RANS is employed. The non-dimensional parameters are as follows:

$$\begin{aligned} x &= x^*/c, \quad z = z^*/c, \\ u &= u^*/a^*_\infty, \quad w = w^*/a^*_\infty, \\ \rho &= \rho^*/\rho^*_\infty, \quad e = e^*/a^{*2}_\infty, \\ t &= t^* c/a^*_\infty, \quad Re = \rho^*_\infty u^*_\infty c/\mu^*_\infty \end{aligned} \tag{2.1}$$

The superscript $*$ is used for dimensional quantities. The subscript ∞ is used for freestream properties and a is the speed of sound, ρ is the density, μ is the viscosity and e is the energy.

The parameters, x and z, are used for along the grid and normal to grid directional lengths and the parameters, *u* and *w*, are used for along the grid and normal to grid directional velocities. Lastly, *c* is the chord length, *t* is the time and the *Re* is Reynolds number.

The strong conservation-law form of the 2-D, thin-layer, Reynolds Averaged Navier-Stokes equations is solved on each subgrid. Using curvilinear coordinates (ξ, ζ) the governing equations of RANS are as follows:

$$\partial_t \hat{Q} + \partial_\xi \hat{F} + \partial_\zeta \hat{G} = Re^{-1}(\partial_\zeta \hat{S}) \tag{2.2}$$

where $\hat{Q}$ is the conservation array, $\hat{F}$ and $\hat{G}$ are convective flux vectors and $\hat{S}$ represents viscous fluxes. The equation is discretized and solved using the third order Osher upwind flux difference splitting method [35, 36]. Detailed equations can be found at Kaya et al. [37, 38].

2.3 Turbulence Model

Turbulence computations are performed using the Spalart Allmaras turbulence model. Spalart and Allmaras [39] described a one-equation model developed for aerodynamic applications, in which a single model transport equation is solved for the turbulent viscosity, ν_t. The model is designed for aerodynamic flows, such as transonic flow over airfoils, including boundary-layer separation [40]. The general form of the equation is;

$$\frac{\partial \nu_t}{\partial t} + \nabla \cdot (\nu_t \vec{V}) = \nabla \cdot \left(\frac{\nu_T}{\sigma_\nu} \nabla \nu_t \right) + S_\nu \tag{2.3}$$

The expanded form of this equation is as follows [39];

$$\begin{aligned} \frac{\partial \tilde{\nu}}{\partial t} + \nabla \cdot (\tilde{\nu} \vec{V}) &= C_{b1}[1 - f_{t2}]\tilde{S}\tilde{\nu} + \frac{1}{\sigma}\{\nabla \cdot [(\nu + \tilde{\nu})\nabla\tilde{\nu}] + C_{b2}|\nabla\nu|^2\} \\ &\quad - \left[C_{w1} f_w - \frac{C_{b1}}{\kappa^2} f_{t2} \right] \left(\frac{\tilde{\nu}}{d} \right)^2 + f_{t1} \Delta U^2 \end{aligned} \tag{2.4}$$

Where $\tilde{\nu}$ is a function of kinematic viscosity (ν) and turbulent viscosity (ν_t) as follows;

$$\nu_t = \tilde{\nu} f_{v1}, \quad f_{v1} = \frac{\chi^3}{\left(\chi^3 + C_{v1}^3\right)}, \quad \chi = \frac{\tilde{\nu}}{\nu} \tag{2.5}$$

and other parameters are given as;

$$\tilde{S} = S + f_{v2}\frac{\tilde{\nu}}{(\kappa^2 d^2)}, \quad f_{v2} = 1 - \frac{\chi}{(1 + \chi f_{v1})}, \quad S = \sqrt{2\Omega_{ij}\Omega_{ij}} \tag{2.6}$$

$$f_w = g\left[\frac{1 + C_{w3}^6}{g^6 + C_{w3}^6}\right]^{1/6}, \quad g = r + C_{w2}(r^6 - r), \quad r = \frac{\tilde{\nu}}{\left(\tilde{S}\kappa^2 d^2\right)} \tag{2.7}$$

$$f_{t1} = C_{t1} g_t \exp\left(-C_{t2}\frac{\omega_t^2}{\Delta U^2}[d^2 + g_t^2 d_t^2]\right) \tag{2.8}$$

$$C_{w1} = \frac{C_{b1}}{\kappa^2} + \frac{(1 + C_{b2})}{\sigma}, \quad f_{t2} = C_{t3} \exp\left(-C_{t4}\chi^2\right) \tag{2.9}$$

The rotation tensor, Ω, is given by;

$$\Omega_{ij} = \frac{1}{2}\left(\frac{\partial u_i}{\partial x_j} - \frac{\partial u_j}{\partial x_i}\right) \tag{2.10}$$

and d is the distance from the closest surface.

The remaining variables; σ, C_{b1}, C_{b2}, κ, C_{w2}, C_{w3}, C_{v1}, C_{t1}, C_{t2}, C_{t3} and C_{t4}, are the constants of this model and for this study following values are used;

$$\begin{aligned} \sigma &= 2/3, & C_{b1} &= 0.1355, & C_{b2} &= 0.622, \\ \kappa &= 0.41, & C_{w2} &= 0.3, & C_{w3} &= 2, \\ C_{v1} &= 7.1, & C_{t1} &= 1, & C_{t2} &= 2, \\ C_{t3} &= 1.1, & C_{t4} &= 2 \end{aligned} \tag{2.11}$$

Two additional assumptions are employed for modeling turbulence with Spalart Allmaras. First assumption is fully turbulent flow assumption, which can be achieved by equating C_{t1} and C_{t3} terms to zero. Second assumption is transition location assumption, where the transition location is defined by the user and before transition location, turbulent viscosity, ν_T, is taken to be zero. In this study, the transition location is defined according to experimental data. If no experimental data exists, the transition location is taken to be at leading edge or fully turbulent flow assumption is employed.

2.4 Boundary Conditions

Three boundary conditions are used; the farfield, the wall and the jet. Since compressible, viscous Navier stokes equations are solved, farfield and wall boundary conditions are straight forward and given below. The jet boundary condition requires special attention. In this study the jet boundary condition is developed and its algorithm is added to in-house RANS solver.

2.4.1 Jet Boundary Conditions

The jet is implemented by imposing the velocity boundary conditions on the wall. In this study, a jet is defined by six parameters; the jet type, the jet velocity (u_{jet}), the jet frequency (F_{jet}), the jet location (x_{jet}), the jet slot width (w_{jet}) and the jet angle (α_{jet}). The parameters are shown in Figure 2.1. As seen in the figure, at the jet location, the jet velocity is given with a velocity profile with the jet angle from the surface of the profile, in the jet slot width.

All jet variables are non-dimensionalized using the chord (c) and free stream speed of sound (a_∞). The non-dimensionalized jet parameters are as follows;

$$\begin{aligned} x_{jet} &= \frac{x^*_{jet}}{c} & w_{jet} &= \frac{w^*_{jet}}{c} \\ u_{jet} &= \frac{u^*_{jet}}{a_\infty} & F^{jet} &= \frac{F^*_{jet}}{a_\infty/c} \end{aligned} \tag{2.12}$$

When modeling the jet velocity three types of profiles are tested; top-hat, *sin* distribution and sin^2 distribution, which are shown in Figure 2.2. Donovan et al. [31] validated these profiles and showed that by using constant momentum coefficient, these three profiles gave almost the same solution of flowfield. However, sin^2 distribution is found to be numerically more stable.

$$\begin{aligned} u_{jet}(s) &= u_{jet}(t) \\ u_{jet}(s) &= u_{jet}(t) sin(\pi s) \\ u_{jet}(s) &= u_{jet}(t) sin^2(\pi s) \end{aligned} \tag{2.13}$$

Three kinds of jet are considered; the steady blowing jet, the pulsed blowing jet and the synthetic jet, which are shown in Figure 2.3. For steady blowing, the mean jet velocity ($u_{mean,jet}$)

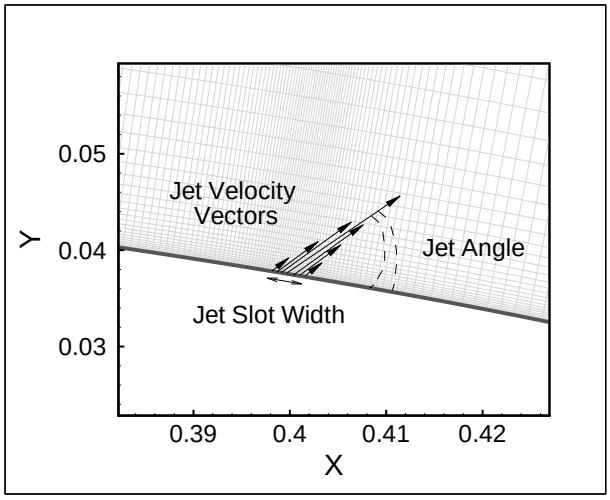

Figure 2.1: Implementation of a Jet

is applied as the wall boundary velocity. The pulsed and synthetic jet periodically actuates the surface. Common approach for modeling this actuation is sinusoidal oscillation of velocity ($u_{osci,jet}$) with the jet frequency. The formulation is given as:

$$u_{jet}(t) = u_{mean,jet} + u_{osci,jet} sin(2\pi F_{jet} t) \tag{2.14}$$

The other parameters being the jet location, the jet slot width and the jet angle are illustrated in Figure 2.1. The jet location is defined as the midpoint between the start and end grid points of the jet and the distance between them is called the jet slot width. The jet angle is defined as the local angle between the surface and the jet velocity.

The jet momentum coefficient ($C_{\mu,jet}$) and the jet power coefficient ($C_{p,jet}$), which are commonly used in flow control studies with jets, are defined as;

$$\begin{gathered} \rho_{jet} = \rho_\infty \\ C_{\mu,jet} = \frac{\rho_{jet} u_{jet}^{*2} w_{jet}^{*}}{\rho_\infty a_\infty^2 c} = u_{jet}^2 * w_{jet} \end{gathered} \tag{2.15}$$

$$\begin{gathered} \rho_{jet} = \rho_\infty \\ C_{p,jet} = \frac{\rho_{jet} u_{jet}^{*2} w_{jet}^{*2} F_{jet}^{*}}{\rho_\infty a_\infty^2 c^2 a_\infty / c} = u_{jet}^2 * w_{jet}^2 * F_{jet} \end{gathered} \tag{2.16}$$

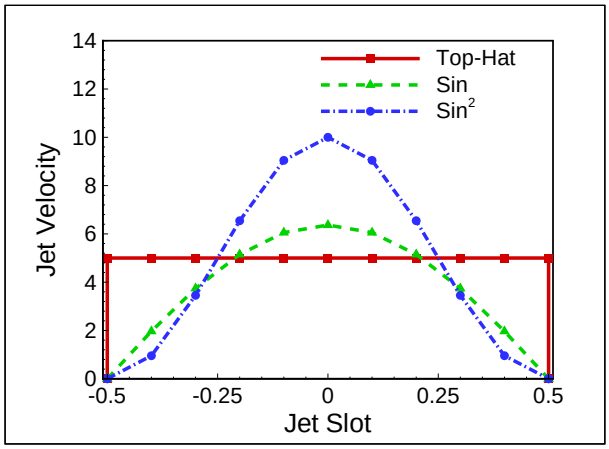

Figure 2.2: The Jet Profiles Used

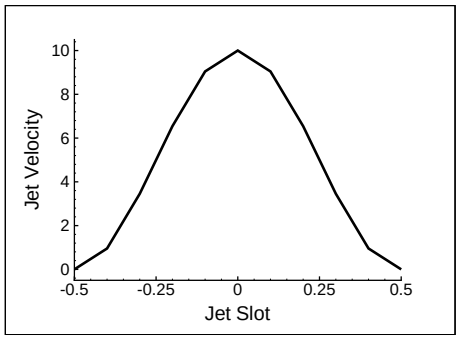

(a) Steady Jet

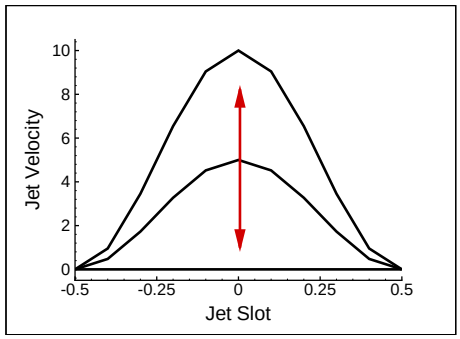

(b) Pulsed Jet

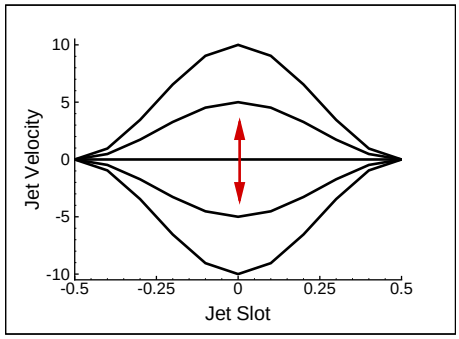

(c) Synthetic Jet

Figure 2.3: Kinds of Jets

2.4.2 Wall Boundary Conditions

Since viscous flow is solved on stationary walls, all the tangential and normal velocity vectors at the wall boundary will be zero except the jet location.

$$u_{cell} = 0 \quad v_{cell} = 0 \tag{2.17}$$

2.4.3 Farfield Boundary Conditions

In this study, farfield boundaries are taken to be 10 chords away from the geometry. Outside the grid, the freestream Mach number and the freestream Reynolds number are defined. Using the Riemann invariants, the non-dimensional grid properties namely pressure, density, energy and velocity, are calculated. However, the grid choice, 10 chords away from the geometry, results in a state where pressure, density and temperature are almost equal to freestream conditions.

The Riemann boundary condition is as follows:

$$\begin{aligned} u + {}^{2a}/_{\gamma-1} &= R^{+} \\ u - {}^{2a}/_{\gamma-1} &= R^{-} \end{aligned} \tag{2.18}$$

where u is the normal velocity, a is the speed of sound, γ is the specific heat ratio, R^{+} and R^{-} are the Riemann invariants. The isentropic assumption, or constant total pressure, is applied and the formulation of Riemann condition is as follows;

$$\begin{aligned} p_{total,k_{max}} &= p_{total,\infty} \\ u_{k_{max}} &= u_{\infty} \\ w_{k_{max}} &= w_{\infty} \\ R^{+}_{k_{max}} &= R^{+}_{\infty} \\ R^{-}_{k_{max}} &= R^{-}_{\infty} \end{aligned} \tag{2.19}$$

where subscript k_{max} denotes the outer most grid, and ∞ denotes the freestream quantities. Using this equation set, pressure, density, grid velocities and energy is computed.

2.4.4 Overlapping Boundary Conditions

In this study, the grid is parallelized by domain decomposition. To have accurate results all partitions have overlapping grids in grid normal (η) direction. Overlapping of η=1 and η=k_{max} is shown in Figure 2.4. Each step overlapping boundary conditions are exchanged.

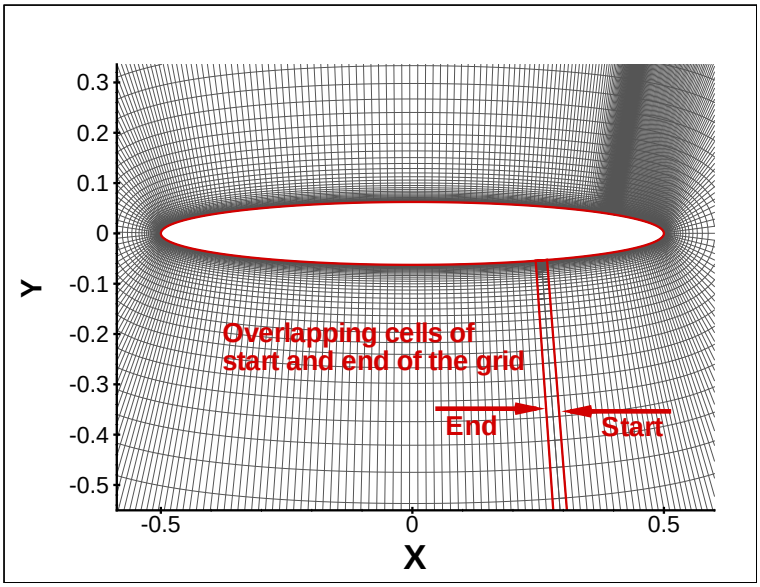

Figure 2.4: Overlapping of first and end cells

2.5 Grid Generation

The elliptic profile chosen for this study is 12.5 % thick and defined by the following formula:

$$\frac{x^2}{1^2} + \frac{y^2}{0.625^2} = 0 \tag{2.20}$$

For solving the jet, fine mesh near jet location is necessary. Grid is refined around the jet location, the leading edge and the trailing edge. Using an in-house algebraic grid generator, the structured, body-fitted grid is formed. The far field boundary is taken about 10 chord lengths away from the profile. The mesh growing factor is chosen to be 1.15. The grid is demonstrated in Figure 2.5, and the concentrated points near jet location are shown in Figure 2.5(b).

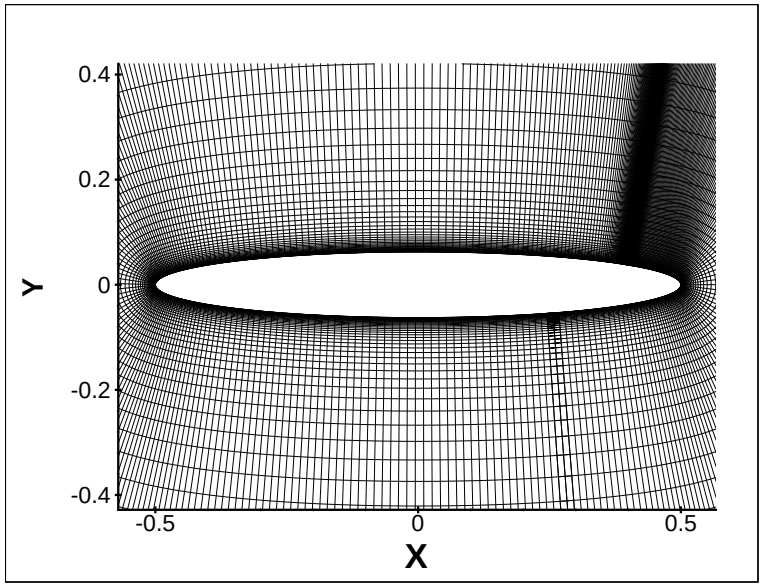

(a)

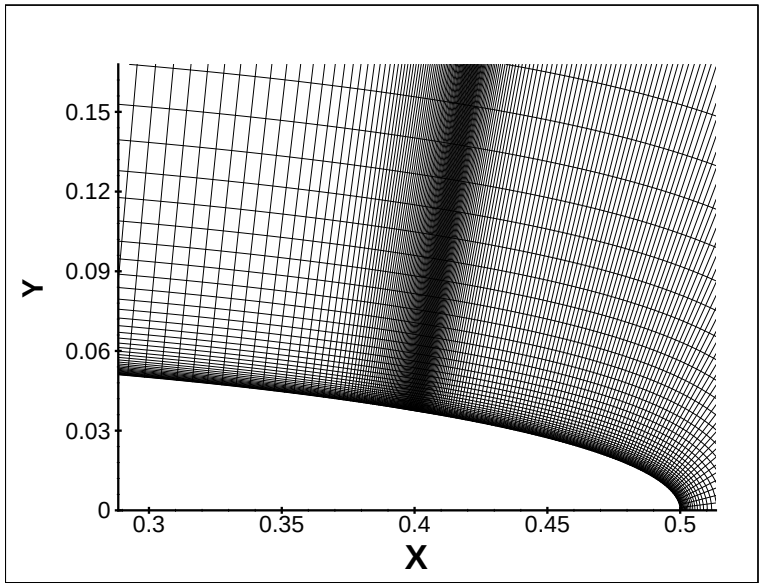

(b)

Figure 2.5: The Grid for 12.5% elliptic profile

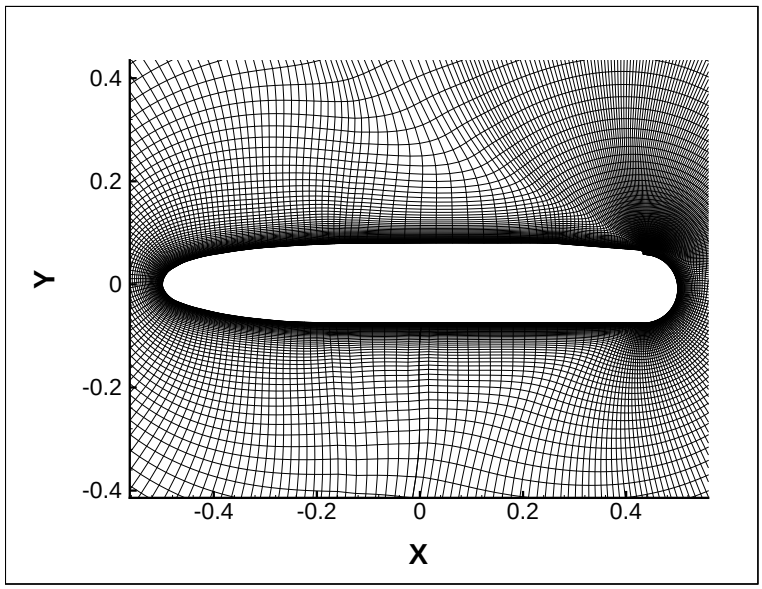

(a)

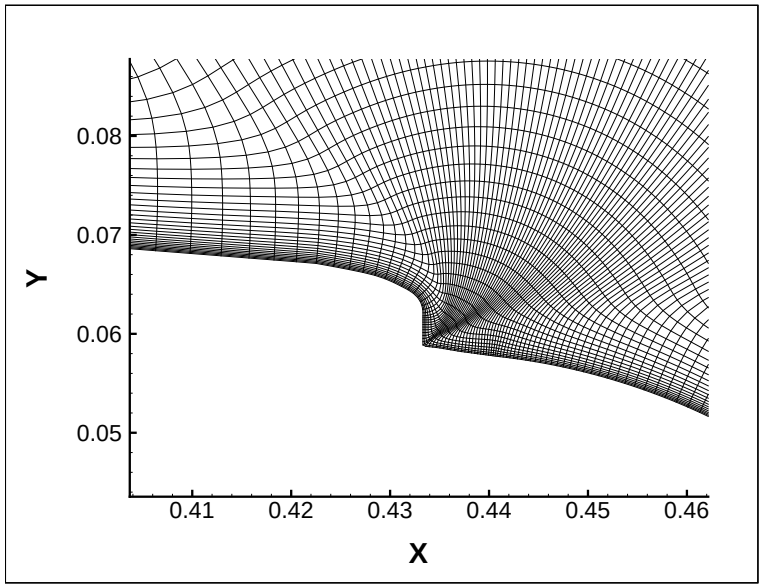

(b)

Figure 2.6: The Grid for 15.6% thick circulation control airfoil

For validation studies, an additional geometry is formed by GRIDGEN. This geometry is 15.6% thick circulation control airfoil. It is defined by an elliptical profile cut at 0.93 chord, a jet slot height added and closed with a circular trailing edge. The grid is presented in Figure 2.6, and the jet slot is shown in Figure 2.6(b).

All the grids used are partitioned for parallel computation. The domain decomposition is discussed in following section.

2.6 Parallel Computation

The parallel computation of flowfield is carried out by decomposing grids in a parallel cluster of computers. Each subgrid is assigned to a processor. PVM [41] (Parallel Virtual Machine) libraries are used for interprocess communication.

In parallel computations there are important issues that need special attention; domain decomposition, load balancing and speed-up. In this study, the domain decomposition is performed by partitioning the grid perpendicular to the elliptic profile. To have accurate results and fast convergence, the partition separation is not located close to the leading edge, trailing edge or the jet slot. Maintaining the computational activity on each processor is known as load balancing. It is desirable to minimize waiting time for the data coming from another processor. In present work, static load balancing is employed, which can be sustained by partitioning the grid equally. Another issue is speed-up. It is defined as how fast the parallel code as compared to a serial code solving the same problem. The parallel routines employed in the same computer cluster for this study, are previously studied by Tuncer et al. [42] for speed-up values. It is shown that after four partitions, increasing number of partitions is not increasing the speed-up value significantly, due to network delays. In this study, two to five partitions is employed according to size of the grid. An example of for grid partitioning is shown in Figure 2.7 for four partitions.

PVM [41] currently supports FORTRAN, C and Java programming languages. In this thesis, Fortran PVM libraries are employed, since RANS solver used is in FORTRAN language. After constructing a cluster of processors, PVM assigns a task to each processor. Processor

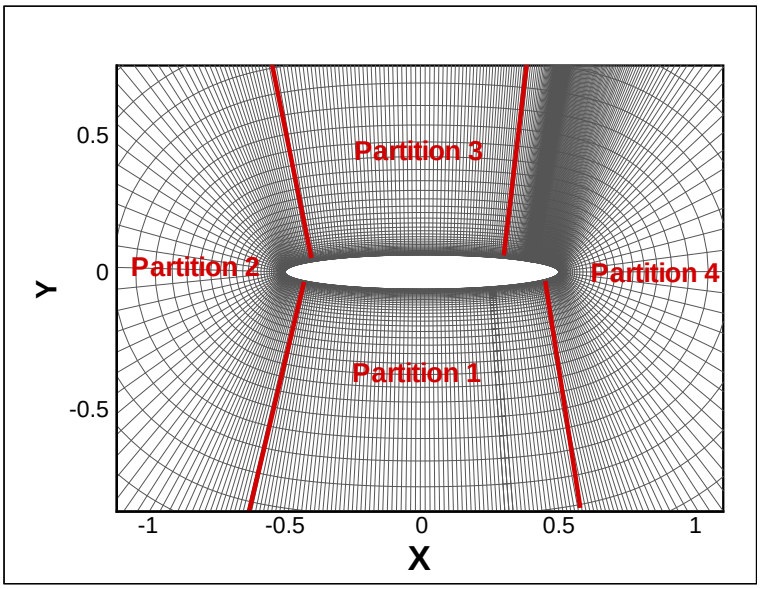

Figure 2.7: The grid having four partitions

communication for sharing data, called interprocess communication, is provided by PVM library routines.

The cluster of computers available includes 6 quad-core Intel processors of 2.33 GHz speed, with 16 GB memory. All computers are running on Linux operating systems. The computers are connected with the 1 Gbps switched Ethernet network.

The parallel algorithm is demonstrated at Figure 2.8. The algorithm contains a master and several workers. The master takes initial conditions and partitions the grid into subdomains. PVM assigns each subdomain to a worker and each worker uses a processor. At each step, overlapping boundary conditions are exchanged between workers using PVM libraries. In predefined periods, the workers send solutions to master. When intended iterations are finished, the master sends all workers a stop message.

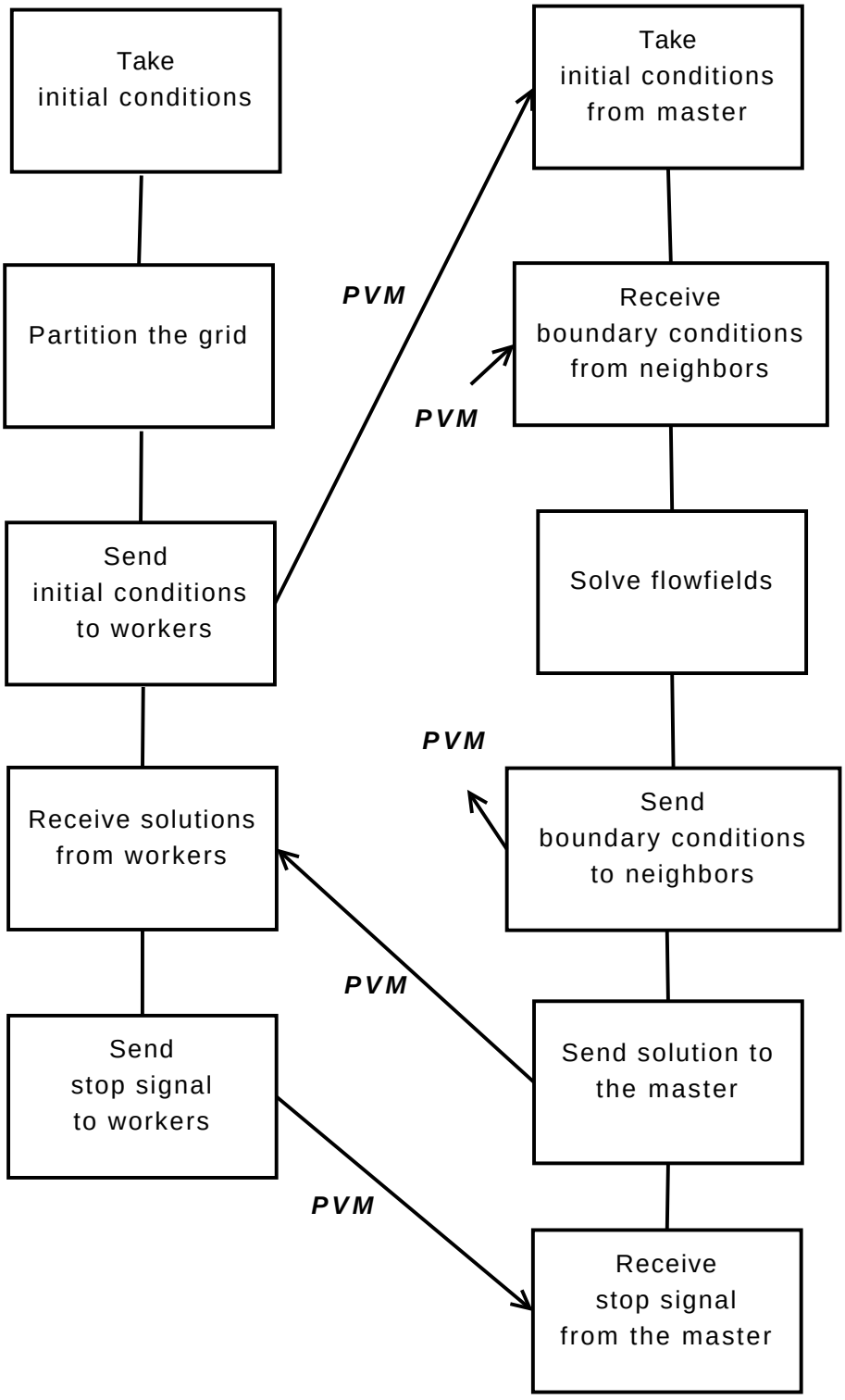

Figure 2.8: Flow chart of parallel algorithm

CHAPTER 3

OPTIMIZATION

3.1 Introduction

The recent experimental and numerical studies investigating blowing jets and synthetic jets show that the drag coefficient is closely related to the jet parameters. The main parameters are the jet velocity, the jet angle, the jet frequency, the jet location and the jet slot width. It is apparent that, in order to minimize the drag coefficient optimization of all these parameters is needed. The optimization tool employed in this study is Response Surface Methodology, based on Least Square approximation. This chapter presents how the Response Surface Methodology is applied for an optimization process to minimize the drag coefficient.

The objective function is taken to be the drag coefficient, and optimization variables are the jet velocity, the jet angle, the jet frequency, the jet location and the jet slot width.

3.2 Response Surface Method

Response Surface Method (RSM) is a technique for fast and efficient optimization to provide a significant insight to complex or unknown systems. RSM is developed to model the response of a complex system using a simplified equation. RSM approximates responses to input parameters with a polynomial function based on a given set of data. This data is obtained at certain set of input conditions, which is produced by various Design of Experiment (DoE) methods. Once response surface is obtained, statistical evaluation is done to assure RSM approximation is good enough. [43, 44]

3.2.1 Formulation

RSM is a Least Squares based method. A given set of data is approximated by a polynomial, whose coefficients are unknown. Using the Least square method, the coefficient matrix (C_i) is determined. [45]

$$Y_i = X_{ij} * C_i + E_i \tag{3.1}$$

Here, Y_i represents the given set of data, X_{ij} represents the input parameters and E_i represents the error that results from approximation. It is necessary to minimize the summation of the error squares.

$$E_i = Y_i - X_{ij} * C_i \tag{3.2}$$

$$S = E_i^2 \tag{3.3}$$

This can be done by equating the gradient of the summation of the error squares to zero.

$$\frac{\partial S}{\partial C_i} = 2E_i \frac{\partial E_i}{\partial C_i} \tag{3.4}$$

$$0 = 2E_i \frac{\partial E_i}{\partial C_i} \tag{3.5}$$

Differentiating E_i in Equation 3.2;

$$\frac{\partial E_i}{\partial C_i} = -X_{ij} \tag{3.6}$$

Then substituting Equation 3.2 and Equation 3.6 into Equation 3.5 gives the following equation.

$$0 = 2(Y_i - X_{ij} * C_i)(-X_{ij}) \tag{3.7}$$

In matrix form it can be illustrated as;

$$(X^T X)C = X^T Y \tag{3.8}$$

and the solution of this matrix equation is

$$C = (X^T X)^{-1} X^T Y \tag{3.9}$$

In this thesis, for simplicity, second order polynomial is used for minimizing the drag coefficient. The optimized jet parameters are jet velocity, jet angle, jet frequency, jet location and jet slot width. The previous studies show that increasing the jet power coefficient decreases the drag coefficient. Therefore, jet power coefficient is held constant in this optimization. The jet power coefficient formula is as follows;

$$C_{p,jet} = u_{jet}^2 * w_{jet}^2 * F_{jet} \tag{3.10}$$

Keeping the jet power constant the jet slot width (w_{jet}) becomes a variable dependent to jet frequency (F^+) and jet velocity (u_{jet}). Then, four independent variables are left which are jet location, jet velocity, and jet angle and jet frequency. The second order optimization objective function can be illustrated as below.

$$\begin{aligned} C_d &= c_1 x_{jet}^2 + c_2 u_{jet}^2 + c_3 \alpha_{jet}^2 + c_4 F_{jet}^2 \\ &+ c_5 x_{jet} u_{jet} + c_6 x_{jet} \alpha_{jet} + c_7 x_{jet} F_{jet} \\ &+ c_8 u_{jet} \alpha_{jet} + c_9 u_{jet} F_{jet} + c_{10} \alpha_{jet} F_{jet} \\ &+ c_{11} x_{jet} + c_{12} u_{jet} + c_{13} \alpha_{jet} + c_{14} F_{jet} + c_{15} \end{aligned} \tag{3.11}$$

3.2.2 Design of Experiment

In the Least Squares method, it should be noted that the size of the given data matrix should be greater than size of the coefficient matrix. For achieving the size of the given data many methods are used, called Design of Experiment [46, 47]. Some of these are;

- *Full Factorial*
- Modified Full Factorials

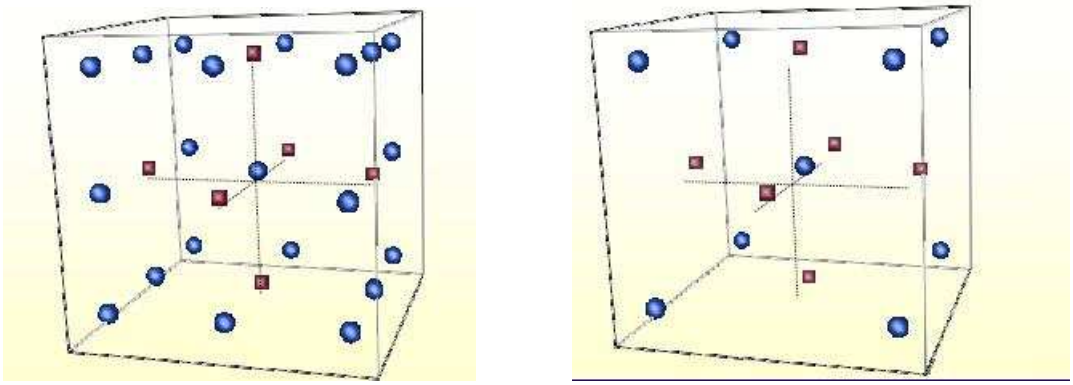

(a) Full Factorial Design Space [46]

(b) Box Behnken Design Space[46]

Figure 3.1: Some Design of Experiment Schemes of RSM

  - Central Composite Design (CCD)
  - Face Center CCD

- Fractional Factorial
- *Box-Behnken*
- Taguchi Orthogonal Arrays
- Latin Hyper Cube

Mavris et al. [46] recommends *Full Factorial* and *Box-Behnken* for second order polynomial RSM approximation. In this thesis, first Full Factorial is employed to figure out the picture and find the first optimum values. Then, in the next iteration, Box-Behnken is used to accelerate the procedure.

Full factorial is a comprehensive method, in which all design space is considered. Three variables design space can be seen at Figure 3.1(a). The number of runs per a RSM set is 3^n, where n is the number of independent variables and 3 is for minimum, maximum and median values of the design space [46, 47].

Box-Behnken design includes less runs, because it covers all the median values and not cover all the corner values. The number of runs is 13 for 3 variables, 25 for 4 variables, 41 for 5 variables. The design space of three variables can be seen at Figure 3.1(b) [46, 47].

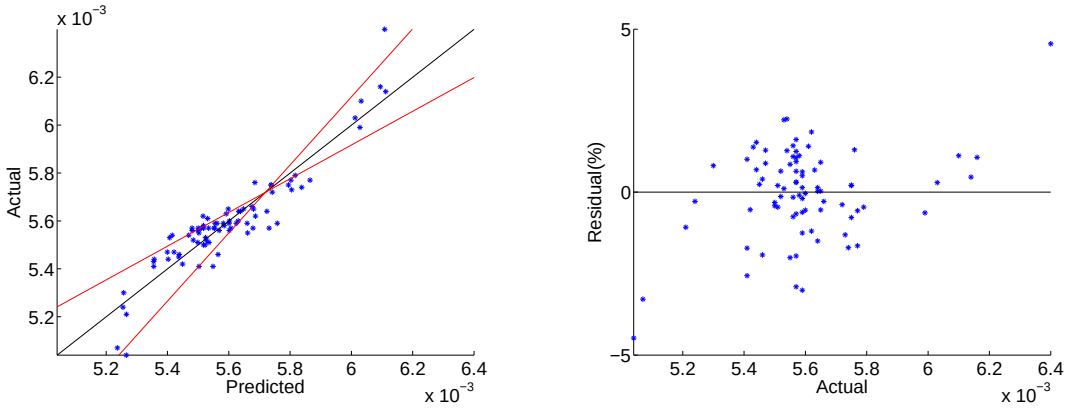

(a) "'Actual vs. Predicted"' (b) "'Actual vs. Error"'

Figure 3.2: Error Plots of RSM

3.2.3 The Fitness of The Achieved Polynomial

For understanding the fitness of the achieved polynomial there are a few statistical values to be checked. These statistical values are defined according to the following terms [46, 47].

- "Actual": Actual data is obtained by the given set of data using the complex system. In current work, complex system is RANS equations, the given set of data is jet parameters and the actual data is the drag coefficient computed from solving the RANS equations in flowfields.
- "Predicted": Predicted data is the response obtained by solving the Least Square problem of RSM using the predefined polynomial and the given set of data. In current work, the predicted data is the drag coefficient and the predefined polynomial is the second order polynomial of jet parameters, as given in Equation 3.11.
- "Error (Residual)": Error or RSM Residual is defined as the difference between "Actual" data and "Predicted" data. This error shows how good the RSM approximated the optimization objective.

The statistical terms are defined as:

- Statistical Significance: Drawing "Actual vs. Predicted" plot, this property can be

checked. The data points should be spread in between 95% confidence lines. An example plot of ”Actual vs. Predicted” is shown in Figure 3.2(a).

- Residual: Drawing ”Actual vs. Error” plot, this property can be checked. The error should be spread and not clumped in specific areas. An example plot of ”Actual vs. Error” is shown in Figure 3.2(b).

In current work, optimization process followed is as follows. First the drag coefficient, actual data, is computed by RANS solver at design space of jet parameters, given set of data. The Least Square problem is solved for the coefficient matrix of second order polynomial. Using the second order polynomial, the drag coefficient is predicted. The Response surfaces of predicted drag coefficient are plotted, as shown in Figure 3.3. The second order polynomial is minimized in the design the space using the *fmincon* routines of MATLAB. The statistical terms defined above are employed for deciding if the optimization objective computed is trustworthy. If one of the statistical terms points out that approximation is not good enough, a smaller design space is formed and the process is restarted from the first step, which is the computation of the drag coefficient by RANS solver.

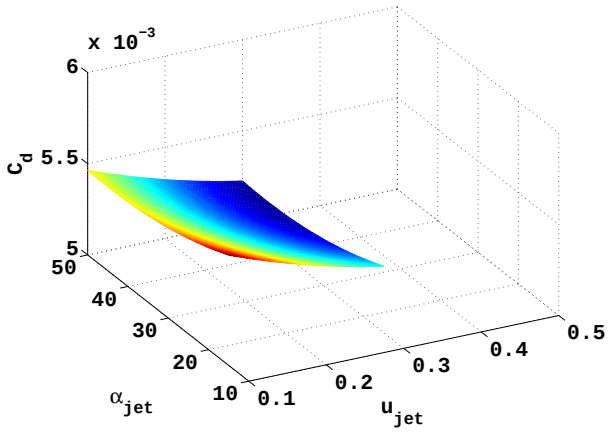

(a)

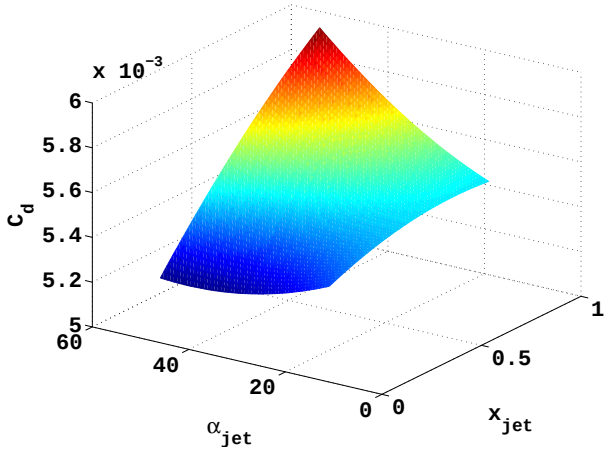

(b)

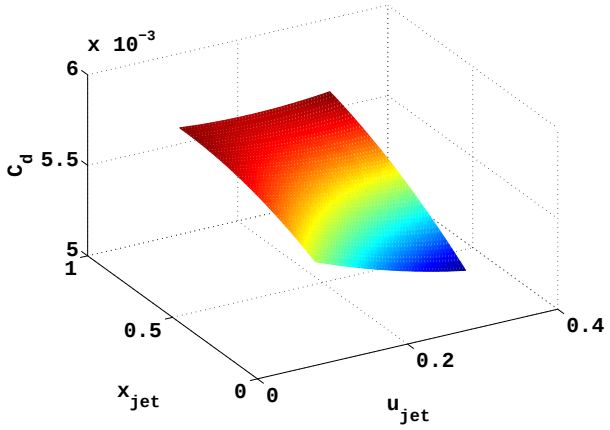

(c)

Figure 3.3: 3D Plots of RSM

CHAPTER 4

RESULTS AND DISCUSSION

4.1 Introduction

Validation studies are performed with/without the presence of the jet. In validation studies, steady blowing and pulsating jets are employed and the Coanda effect is studied. Preliminary studies for the steady blowing, the pulsating and the synthetic jets are performed. Finally, the synthetic jet parameters are parameterized and optimized to minimize the drag.

Unsteady computations are carried out until a steady or a periodic flow solution is obtained. The computed flowfields are analyzed in terms of aerodynamic loads, the average distribution of pressure, the average and instantaneous streamlines. The flows computed are at turbulent regime between Re=0.78x10^6 to Re=1x10^6. In turbulent flow calculations, Spalart-Allmaras turbulence model is employed. Flows with laminar-turbulent transition and fully turbulent flows are analyzed.

The parallel computation of flowfields is carried out by decomposing the structured grid system into subdomains, each of which is assigned to a core. Parallel processing is performed in a cluster of computers with quad-core Intel processors of 2.33 GHz speed running on Linux operating systems. The computers are connected with the 1 Gbps switched Ethernet network. PVM library routines are used for interprocess communication.

For validation studies, except the Coanda effect study, the comprehensive study of Sohn et al. [48] is used. This experimental study is performed over a 12.5% thick elliptical wing in a wind tunnel. The elliptical wing has a chord of 0.4m and a span of 1.5 m. The flow conditions in the wind tunnel are given as the freestream velocity of 30 m/s, Mach number of 0.1 and

Reynolds number of 822000. Cases without a jet, with a steady blowing jet and with a pulsed blowing jet are analyzed using pressure measurements and smoke lines photographs. The pressure data is collected by 40 pressure taps on the upper surface of the profile on the mid span. Without the presence of the jet, the pressure data is collected for angles of attack 0^o to 20^o. With the presence of the jet, the pressure data is collected for angles of attack 12^o to 20^o. On the wing there are two jet slots, with widths of 1mm and lengths of 1m, which are located at the leading edge and the trailing edge. With the average jet velocity of $3u_\infty$, two jet angles, 30^o and 90^o, are tested. The pulsed blowing jet is applied with 6 Hz frequency.

4.2 Validation without the Jet

In order to assess numerical accuracy of the computed flowfields, flow solutions are compared with the experimental study of Sohn et al. [48]. Flow solutions are obtained at an angle of attack (α) of 14 degrees, a freestream Mach number (M) of 0.1 and Reynolds number (Re) of 822000, which are the conditions of the experimental study. Grid independence study is performed first. Then, validation studies are carried out with and without a laminar-turbulent transition.

4.2.1 Grid Independence

In order to ensure that flow solutions are independent from the grid size, a grid independence study is conducted in two parts where the grid density along and normal to the wall boundary are varied. Three grid densities along the wall boundary and four grid densities normal to the wall boundary are considered.

Numerical solutions with the grid densities normal to the wall boundary are conducted according the first cell sizes with $1x10^{-3}$, $5x10^{-4}$, $1x10^{-4}$ and $5x10^{-5}$, which correspond to 53, 58, 67 and 74 grids in normal direction. In terms of the dimensionless wall distance (y^+) these thicknesses correspond to 10, 5, 1 and 0.5 respectively. The grid density is kept constant as 322 (medium) in all grids. Average pressure distributions for these grid densities normal the wall boundary are given in Figure 4.1. As observed, the y^+ of 1 and 0.5 have similar the average pressure distributions. The solution is converged to fixed solution at y^+ of 1. This result is an expected result since it is known that flow solutions with y^+=1 gives accurate flow

solutions for the Spalart Allmaras Turbulence Model.

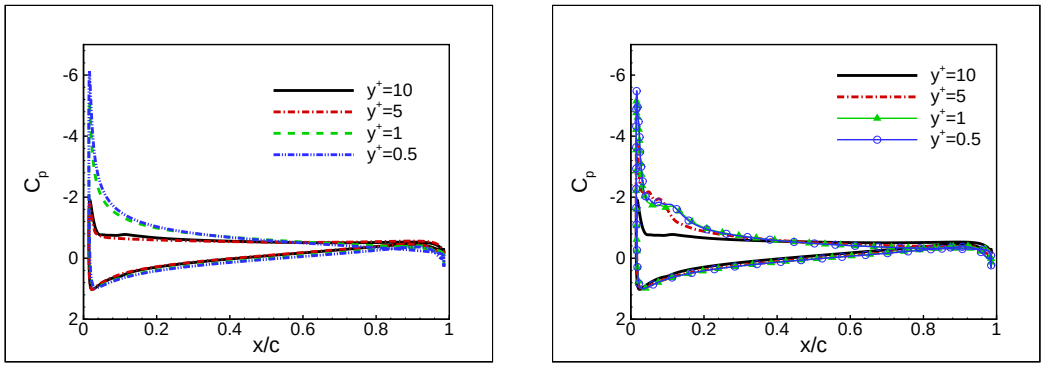

(a) Fully Turbulent Flow (b) Transition location at $x/c = 0.1$

Figure 4.1: Variation of the average pressure distributions with grid densities normal to the wall boundary

Numerical solutions with grid densities along the wall boundary are conducted with 166 (coarse), 322 (medium) and 428 (fine) grids. The first cell size in the surface normal direction is kept constant in all grids as $1x10^{-4}$ or the dimensionless wall distance (y^+) of 1. The average surface pressure distributions computed for these grid densities along the wall boundary are given in Figure 4.2. As seen, the medium and the fine grid densities produces nearly same the average pressure distributions. The solution with the medium grid, with 322 cells, is taken as the grid independent solution.

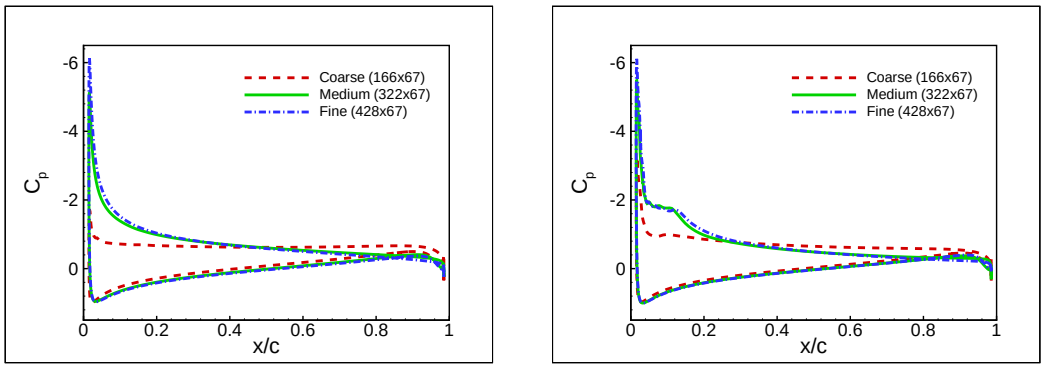

(a) Fully Turbulent Flow (b) Transition location at $x/c = 0.1$

Figure 4.2: Variation of the average pressure distributions with grid densities along the wall boundary

4.2.2 Transition Location

To investigate the effect of transition location on the numerical solution, the transition location is estimated and compared with the fully turbulent flow. Both solutions are validated with the experimental study of Sohn et al. [48].

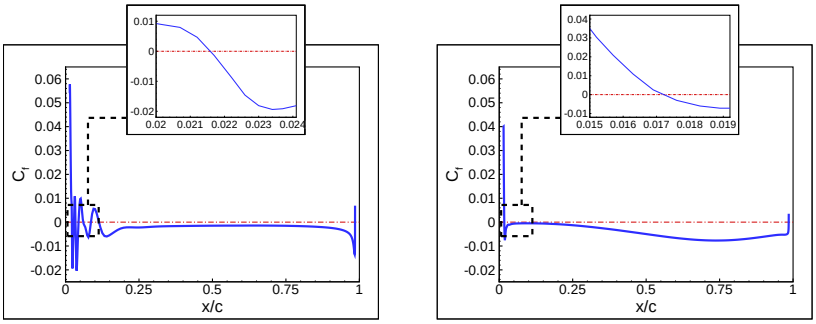

(a) Transition location of $x/c = 0.1$ (b) Fully turbulent flow

Figure 4.3: Skin friction coefficients at maximum C_d instant

The skin friction coefficients at maximum the drag coefficient (C_d) for the transition location at $x/c = 0.1$ and the fully turbulent flows are given in Figure 4.3. The instantaneous flowfields at maximum the drag coefficient (C_d) instant for the transition location at $x/c = 0.1$, the fully turbulent flow and the experimental study [48] are given in Figure 4.4. As seen from Figure 4.3(b) and Figure 4.4(b), for the fully turbulent flow, a flow separation is initiated at $x/c = 0.017$ and from Figure 4.3(a) and Figure 4.4(a), which is the flow with transition location of $x/c = 0.1$ flow, a flow separation starts at $x/c = 0.0215$. As observed in Figure 4.4(c), the smoke lines of experiment shows a flow separation initiated at the leading edge ($x/c = 0.0$). Both flows agree well with the experimental study [48]. The disagreement at the trailing edge is seen from the both figures, Figure 4.4(a) and Figure 4.4(b), the separated flow reattaches to the surface at the trailing edge, where Figure 4.4(c) shows a fully separated flow.

Figure 4.5 compares the average pressure distributions along the profile chord for two transition locations, the fully turbulent flow and the experimental study [48]. As it is seen here, the transition location of $x/c = 0.1$ and fully turbulent flow show a better agreement with the experimental study near the leading edge.

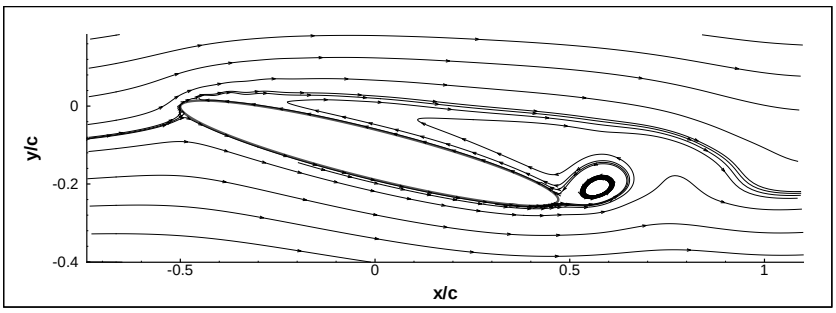

(a) Transition location $x/c = 0.1$

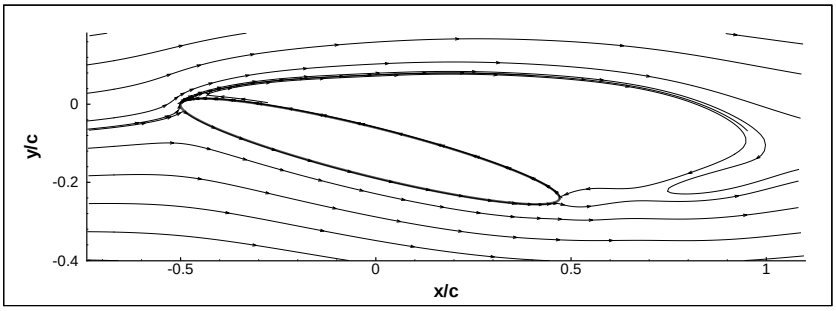

(b) Fully turbulent flow

(c) Experimental data [48]

Figure 4.4: Instantaneous flowfields at maximum C_d instant

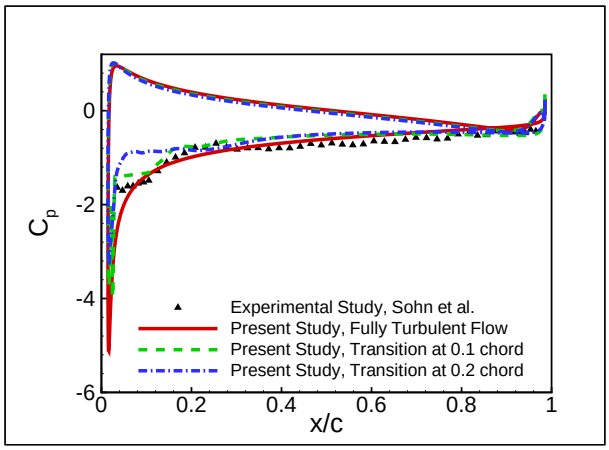

Figure 4.5: Variation of the average pressure distributions

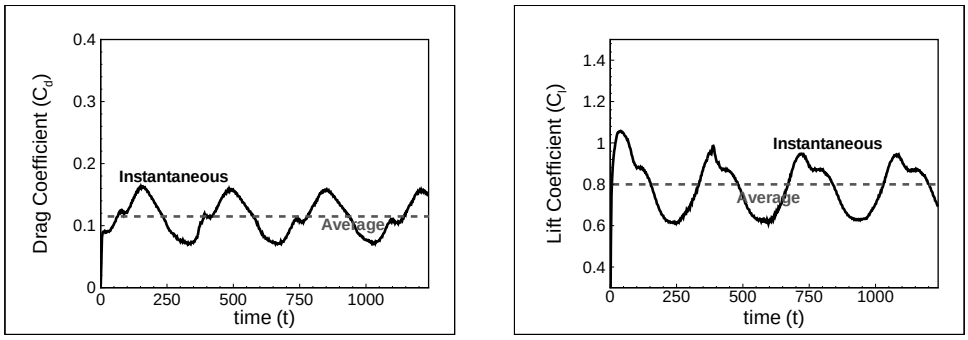

(a) (b)

Figure 4.6: The lift and the drag coefficient histories of the flow with transition location of $x/c = 0.1$

The lift and the drag coefficient (C_l and C_d) histories of the flow with transition location of $x/c = 0.1$ are shown in Figure 4.6. As it is seen from Figure 4.6(a) and Figure 4.6(b), load variations are periodic and two natural frequencies exist. Based on the Fourier analysis, these frequencies are computed as 0.00275 and 0.0154. The average C_d and C_l are computed with the transition location of $x/c = 0.1$ as 0.115 and 0.8, respectively.

Figure 4.7 shows the lift and the drag coefficient histories of the fully turbulent flow. As it is observed from Figure 4.7(a) and Figure 4.7(b) three natural frequencies exist. Based on the Fourier analysis, these frequencies are computed as 0.00275, 0.0154 and 0.033, two of which are the same as natural frequencies of the transition location $x/c = 0.1$. The average C_d and

C_l are computed with fully turbulent flow as 0.125 and 0.81, respectively, which are slightly less than the C_l and C_d of the flow with transition location of $x/c = 0.1$.

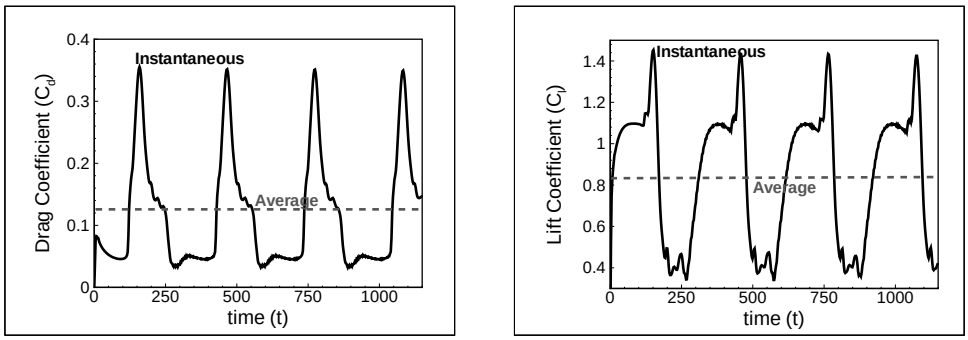

(a) (b)

Figure 4.7: The lift and the drag coefficient histories of the fully turbulent flow

To summarize this subsection, the solution is shown to be grid independent in wall along and wall normal directions. Transition location for angle of attack 14 degrees is estimated as $x/c = 0.1$, since it provides the best agreement with the experimental data.

4.3 Validation with Presence of the Jet

To evaluate the numerical accuracy of the computed flowfields, validation studies with presence of the jet are conducted in three parts. In the first part, the grid independence of steady jet implemented flowfields is shown and validation of various jet profiles is performed. In second part, a pulsed jet is implemented and validated against the experimental data available. In third part, the Coanda effect is validated by solving flowfields achieved by implementing a steady jet near the trailing edge of an elliptic profile.

4.3.1 Steady-Blowing Jet

Flow solutions are obtained at an angle of attack of 14 degrees, a freestream Mach number of 0.1 and Reynolds number of 822000. The steady blowing jet is defined by an average jet velocity of $3u_\infty$, jet slot width of 0.0025c, jet angle of 30^o and a jet location of $x/c = 0.01$. Grid independence study is performed first, to have fast and accurate solutions. Then,

validation studies are carried out by employing various jet profiles, which are explained in section 2.4.1 and shown in Figure 2.2.

4.3.1.1 Grid Independence Study

To show that flow solutions are grid independent, grid independence study is conducted by varying the grid density along the jet slot width. The grid density along the jet slot width is tested with 6, 10 and 20 cells. Variation of the average pressure coefficients for these grid densities along the jet slot width are given in Figure 4.8. As seen from the figure, neither solution differs significantly from the other. The jet slot width is resolved about 10 cells throughout this study.

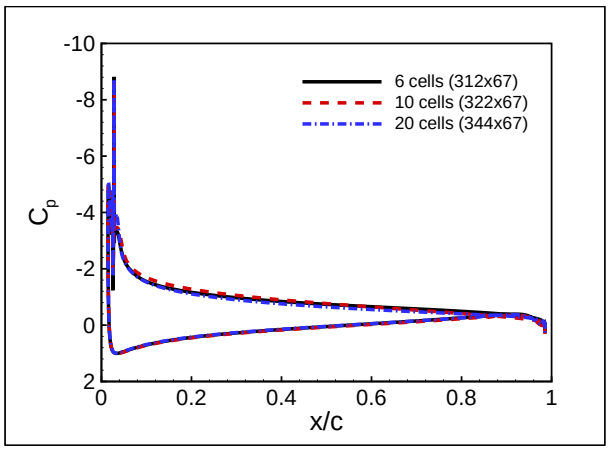

Figure 4.8: Variation of the average pressure coefficient

4.3.1.2 The Jet Profile Study

To provide numerical stability and accuracy, various jet velocity profiles are considered. By keeping the jet momentum coefficient constant, all flow solutions are validated against the experimental study of Sohn et al. [48].

Average flowfields without the jet and with presence of the jet with various jet velocity profiles are shown at Figure 4.9. As seen from Figure 4.9(a), a flow separation starts at $x/c = 0.01$. As observed from figures 4.9(b), 4.9(c) and 4.9(d), all the jet velocity profiles have a good

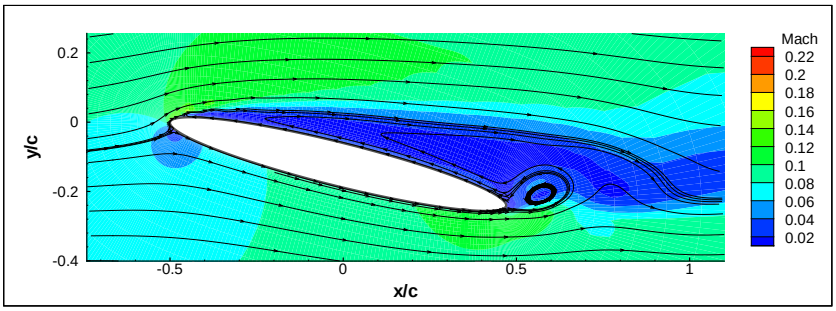

(a) Without jet

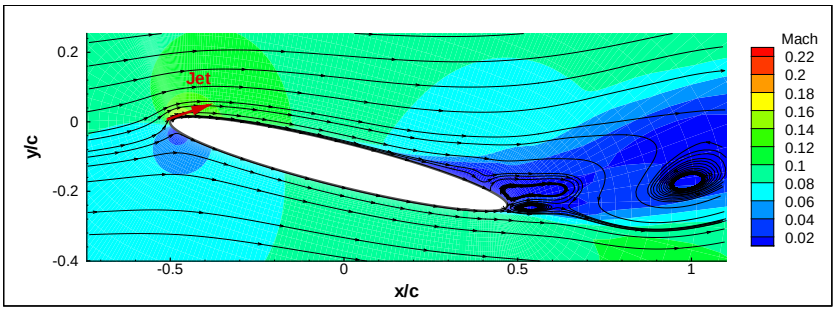

(b) Top-Hat distribution

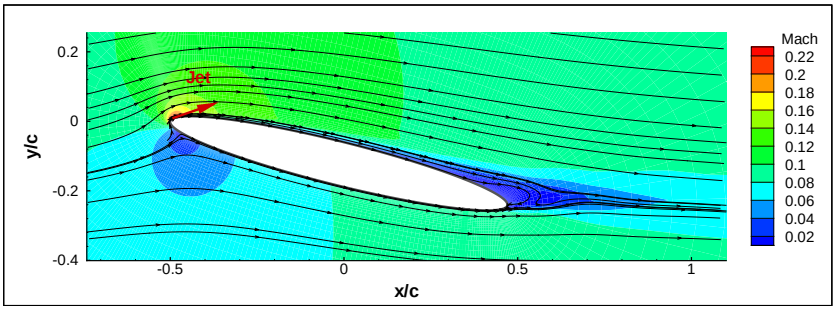

(c) *sin* distribution

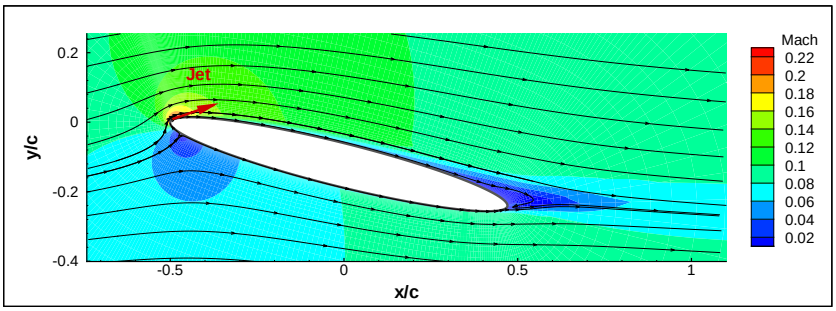

(d) sin^2 distribution

Figure 4.9: Average flowfields for various jet velocity profiles

agreement with each other, the flow is attached to the surface until x/c =0.9. However, top-hat distribution jet is least effective as compared to other jet profiles. It is observed that the application of steady jet delayed the flow separation.

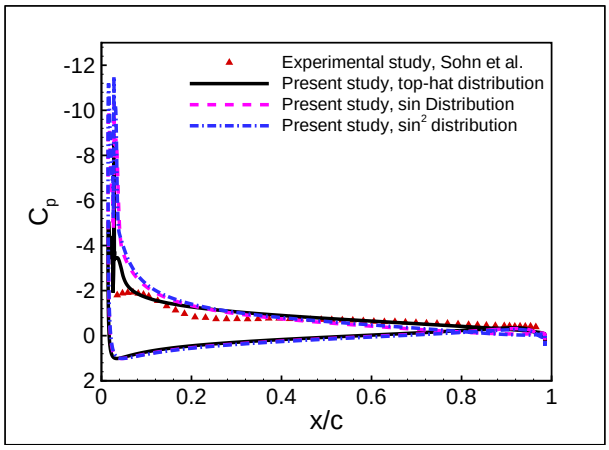

Figure 4.10: Variation of the average pressure coefficients for various jets velocity profiles

Figure 4.10 compares the average pressure coefficients of various jet velocity profiles against the experimental study [48]. As observed from the figure, the jet profiles do not show a significant difference and all the profiles show a good agreement with the experimental study [48]. However, the top-hat distribution jet is least effective as compared to the other jet profiles. Application of the steady jet increased the suction pressure at the leading edge.

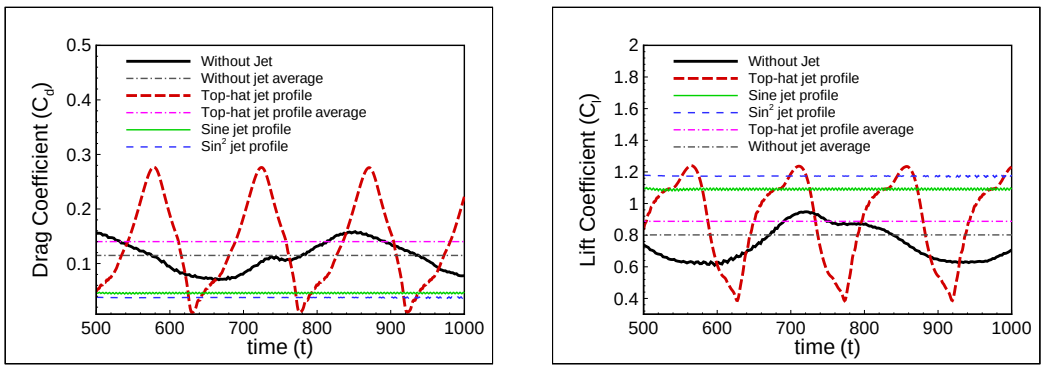

(a) (b)

Figure 4.11: The lift and the drag coefficient histories of various jet profiles

The lift and the drag coefficient histories with and without the presence of the jet for various jet profiles are given in Figure 4.11. As seen from Figure 4.11(a), the application of the jet

reduces the C_d with *sin* and sin^2 profiles. However, the top-hat profile increases the average C_d and the amplitude of oscillations. The average C_d is computed for the top-hat profile, the *sin* profile and the sin^2 profile as 0.14, 0.05 and 0.04 respectively. As seen from Figure 4.11(b), the application of the jet increases the C_l. However, top-hat profile increases the amplitude of oscillations. The average C_l is computed for the top-hat profile, the *sin* profile and the sin^2 profile as 0.88, 1.1 and 1.18 respectively. As observed from the both figures, the sin^2 profile shows a numerical stability and has a stronger influence on the C_l and the C_d.

To summarize this subsection, it is seen that the jet slot width grid resolution with 10 cells provides a grid independent solution. Three jet profiles, with same jet momentum coefficients, are tested, all agree well with the experimental data. In addition, steady blowing jet near leading edge causes the lift enhancement and the drag reduction at the same time. Moreover, it is observed that sin^2 profile causes a steady flow and has a stronger influence on the lift and the drag .

4.3.2 Pulsating Jet

To investigate the effects of the pulsating jet on the flow, a pulse-blowing jet is applied from the leading edge, which is explained in section 2.4.1 and shown in Figure 2.3. The unsteady flows are validated against experimental data of Sohn et al. [48].

Flow solutions are obtained at an angle of attack of 14 degrees, a freestream Mach number of 0.1 and Reynolds number of 822000. The pulsating jet is defined by a maximum jet velocity of $6u_\infty$, jet slot width of 0.0025c, jet angle of 30^o, a jet location of 0.01c and a jet frequency of 0.08. Validation studies are carried out using flowfields and the average pressure coefficient distributions.

The instantaneous flowfields for the present study and the experimental study [48] with the presence of pulsating jet are presented in Figure 4.12. As seen from the figure, the application of pulsating jet causes vortex formation, translation of vortices and reattachment of the flow periodically. As observed, the present study shows a good agreement at the first and the second phases of the period, however, at the third and fourth phases of period, some disagreement exists. Due to the fact that the pulsating jet used by experimental study [48] is a square wave blowing jet and the pulsating jet used by present study is a sine-wave blowing jet, and

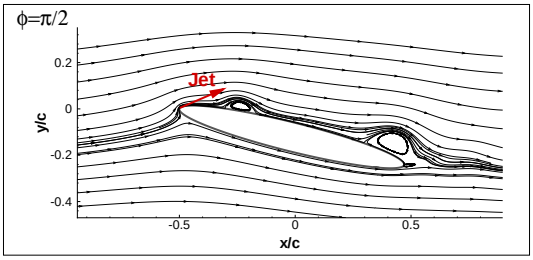

(a) Present

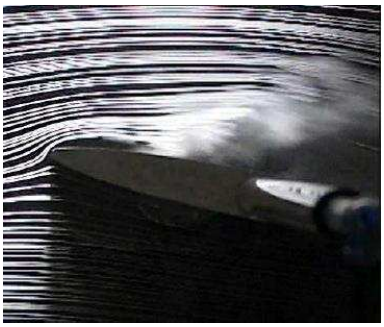

(b) Sohn et al. [48]

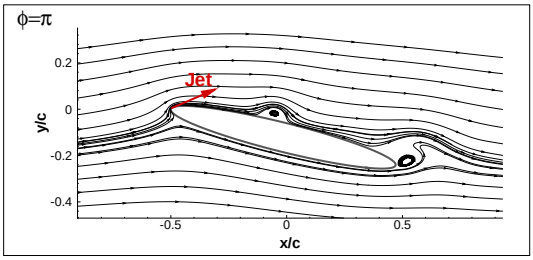

(c) Present

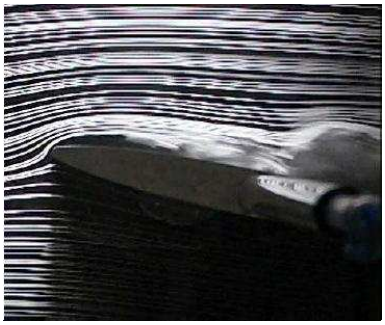

(d) Sohn et al. [48]

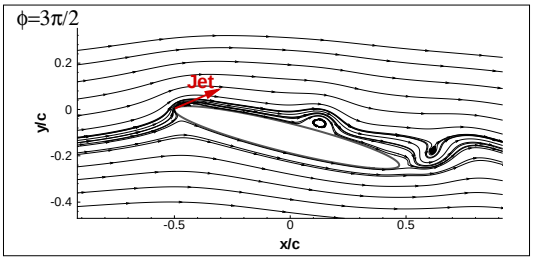

(e) Present

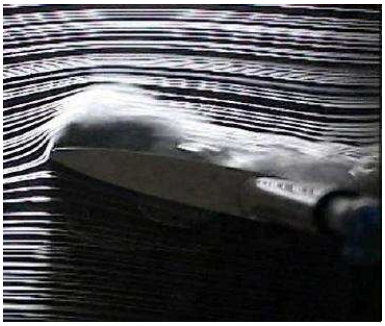

(f) Sohn et al. [48]

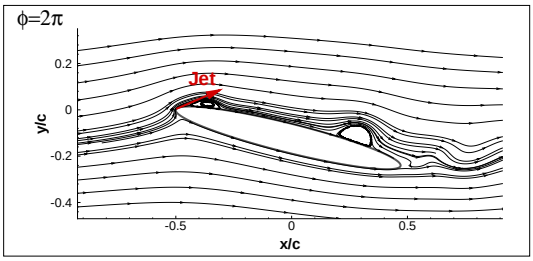

(g) Present

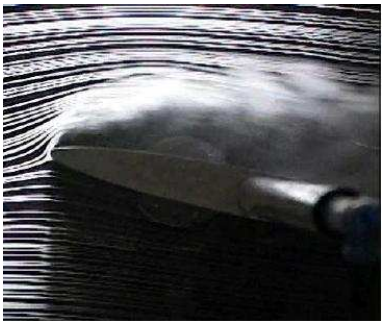

(h) Sohn et al. [48]

Figure 4.12: The instantaneous flowfields with the presence of pulsating jet

since the phases of the experimental study [48] are not stated exactly, there could be some time shift.

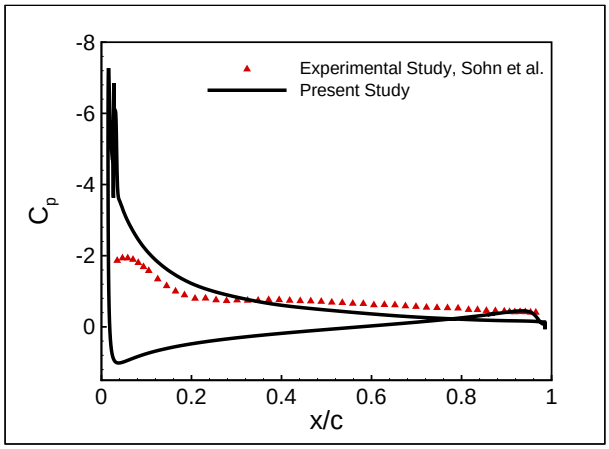

Figure 4.13: Variation of the average pressure coefficient distributions

Figure 4.13 compares the present study and the experimental study [48] in terms of the average pressure coefficients, with the pulsating jet. As seen, the present study overestimates pressure coefficient when compared with the experimental data [48]. It may be attributed to the underestimation of the flow separation in the numerical solutions. In addition, the sin^2 distribution of the jet velocity on the jet slot width is employed, which is shown to be overestimating the pressure coefficient in steady jet validation studies.

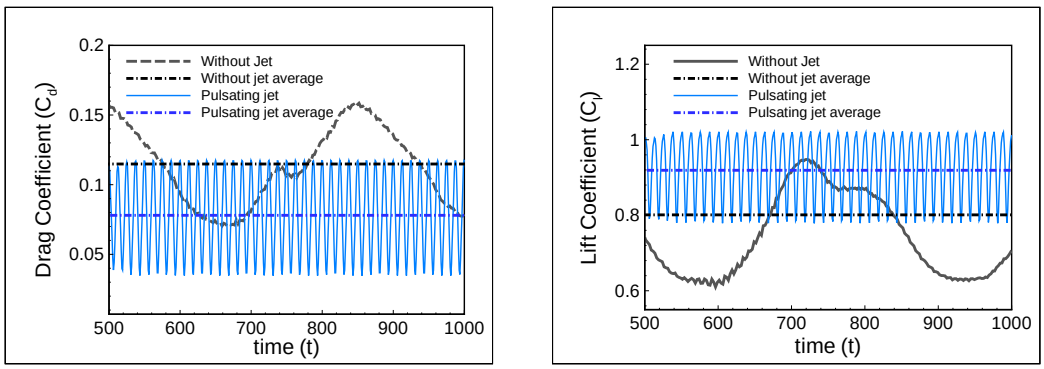

(a) (b)

Figure 4.14: The lift and the drag coefficient histories of the pulsating jet

The lift and the drag coefficient histories are presented for the pulsating jet in Figure 4.14. As seen from the figure, the application of the pulsating jet increases the average C_l from 0.8

to 0.92 and decreases the average C_d from 0.125 to 0.078. With the implementation of the pulsating jet, the amplitude of oscillations is reduced from 0.41 to 0.3 for C_l and from 0.08 to 0.06 for C_d. The frequency of the oscillations for the pulsating jet is equal to the jet frequency of 0.08, which is greater than the frequency of the oscillations for the case without the jet, 0.00275.

To summarize this subsection, it is seen that the influence of pulsating jets are predicted well in general, as compared to the experimental data. However, at instantaneous flow, comparison shows difference since pulsating jets are square waves and the solver uses sine waves to approximate it. Another observation is, applying pulsating jet causes a periodic flow, which has the same frequency with the pulsating jet.

4.3.3 Coanda Effect

In order to investigate the Coanda effect, a blowing jet is applied near the trailing edge and unsteady flow computations are performed. Steady flows are compared with the experimental and the numerical studies of Shrewsbury et al. [2].

In this investigation, a thicker profile with 15.6% thickness is employed. Flow solutions are obtained at an angle of attack of 0 degrees, a freestream Mach number of 0.0853 and Reynolds Number of $0.78\text{x}10^6$. Steady blowing jet is defined by a maximum jet velocity of $5u_\infty$, a jet slot width of 0.004c, jet angle of 90^o, a jet location of $x/c = 0.931$. The geometry, the flow conditions and the jet parameters are taken from the Shrewsbury et al. [2].

In Figure 4.15, the instantaneous flowfields are shown for the present study, with and without the jet, and for numerical study [2] with presence of the jet. As seen from Figure 4.15(a), a flow separation starts at 0.9 chord and vortex shedding occurs at the trailing edge, without the jet. As observed from Figure 4.15(b), the flow is fully attached, with the application of the jet. Figure 4.15(c) and Figure 4.15(b) compares the instantaneous flowfields for the present study and the numerical study [2]. The flowfields of the present study shows a good agreement with the flowfields of the numerical study [2].

In Figure 4.16, the instantaneous pressure distributions are illustrated for the present study, the numerical study [2] and the experimental study [2]. As seen, in the present study the C_p in

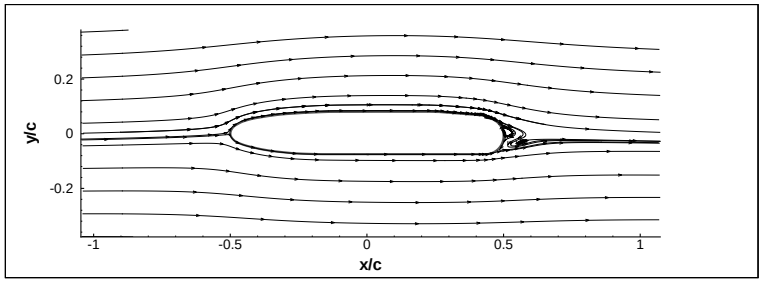

(a) Present study, without jet

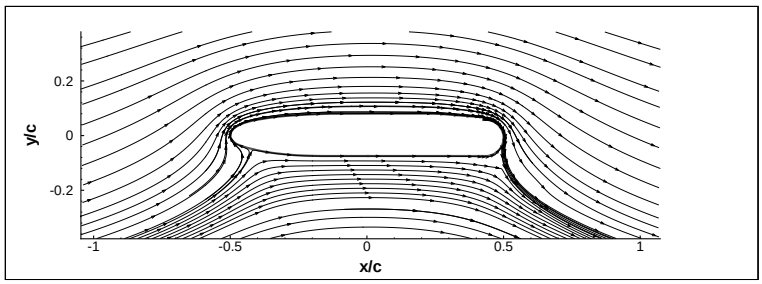

(b) Present study, with jet

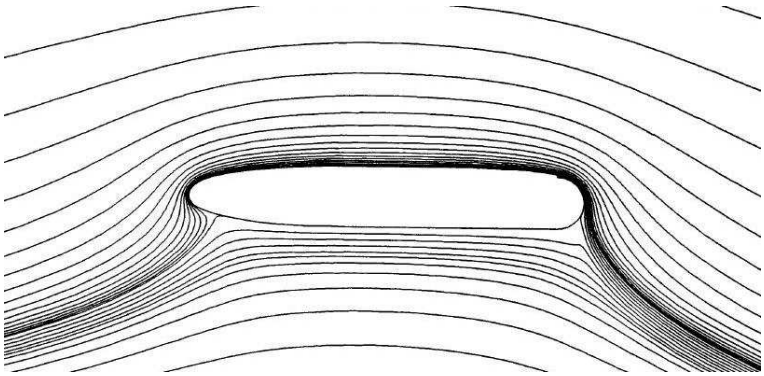

(c) Numerical study [2], with jet

Figure 4.15: The instantaneous flowfields of present study and numerical study [2]

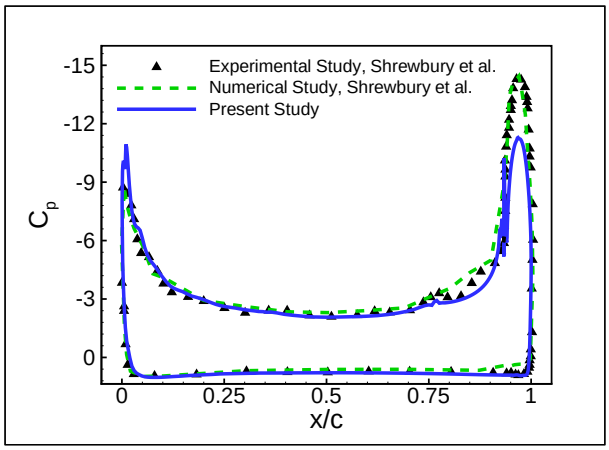

Figure 4.16: Variation of instantaneous pressure distributions

upper part of profile near trailing edge is underestimated as compared to the numerical study [2] and the experimental study [2]. However, in the lower part of profile near trailing edge, the present study shows a better agreement with the experimental study as compared to the numerical study.

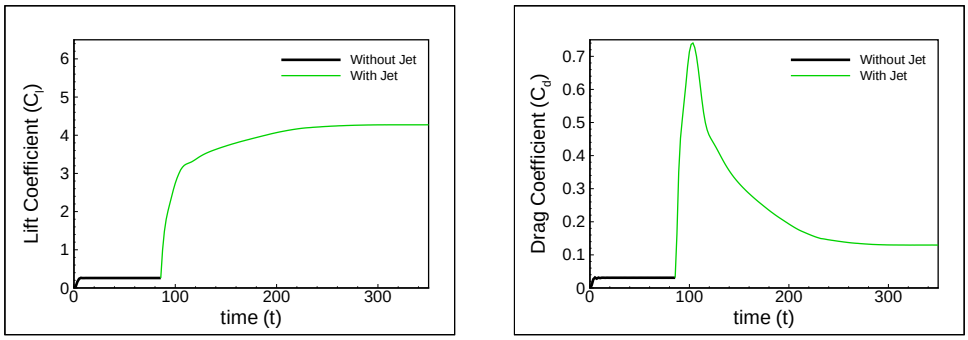

(a) (b)

Figure 4.17: The lift and the drag coefficient histories

The lift and the drag coefficient histories are presented in Figure 4.17. As seen from Figure 4.17(a), application of the jet significantly increases the lift. As observed from Figure 4.17(b), presence of the jet increases the drag . In the present work, the lift coefficient is computed as 4.3, which is close to the value computed in the numerical study of Shrewsbury et al. [2], being 4.5. The drag coefficient is computed as 0.12.

To summarize this subsection, it is seen that Coanda effect causes a large increase in the lift and increases the drag . The prediction agrees well the experimental and numerical data. However, the solutions are shown to be underestimating the suction pressure at the trailing edge, when compared with the experimental data available.

4.4 Preliminary Studies with various jet types

The comparison of three types of jet is carried out to assess the effects of various jets on the flow. Three types of jets are tested; steady blowing, pulsating and synthetic jet, which are explained in section 2.4.1 and shown in Figure 2.3. Flow solutions are obtained at an angle of attack of 14 degrees, a freestream Mach number of 0.1 and Reynolds number of 822000. The jets are defined by a maximum jet velocity of $6u_\infty$, a jet slot width of 0.0025c, a jet angle of 30^o, a jet location of 0.01c and for pulsating jet and synthetic jet, a jet frequency of 0.08. The comparison studies are carried out using flowfields and the lift-the drag time histories.

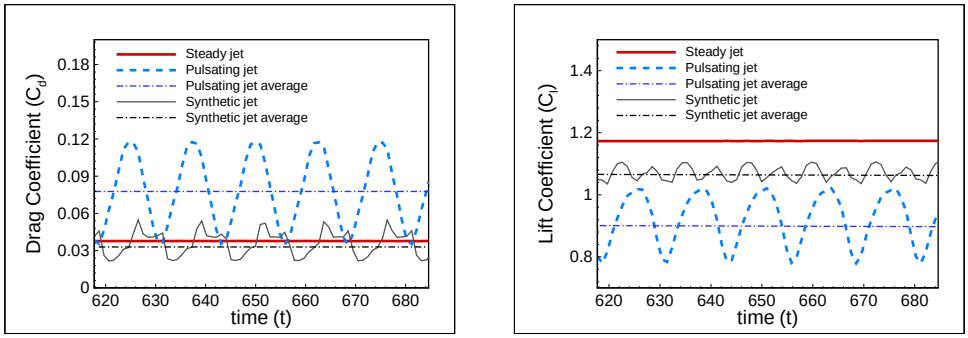

(a) (b)

Figure 4.18: The lift and the drag coefficient histories of various jets

The lift and the drag coefficient histories with presence of various jets are given in Figure 4.18. As seen from Figure 4.18(a), the minimum the drag coefficient is achieved by the synthetic jet. As observed from Figure 4.18(b), the maximum the lift coefficient is achieved by the steady jet. As compared to the pulsating jet, the synthetic jet has the same frequency of oscillations and reduced amplitude of oscillations. In this study, the synthetic jets are employed since previous studies has shown that synthetic jets are smaller and need less power, also the objective of this thesis is minimize the drag .

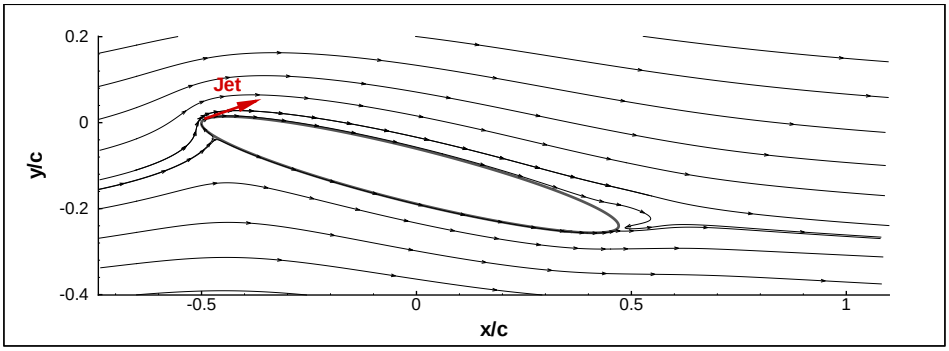

(a) Steady Jet

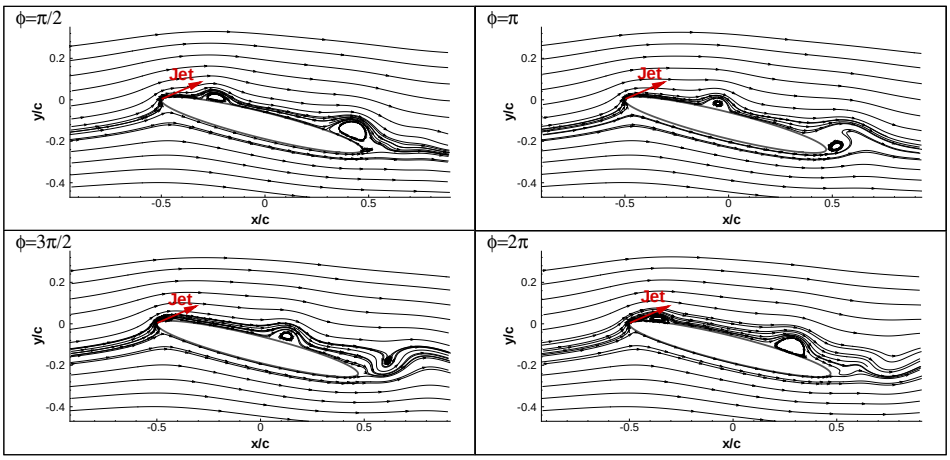

(b) Pulsating Jet

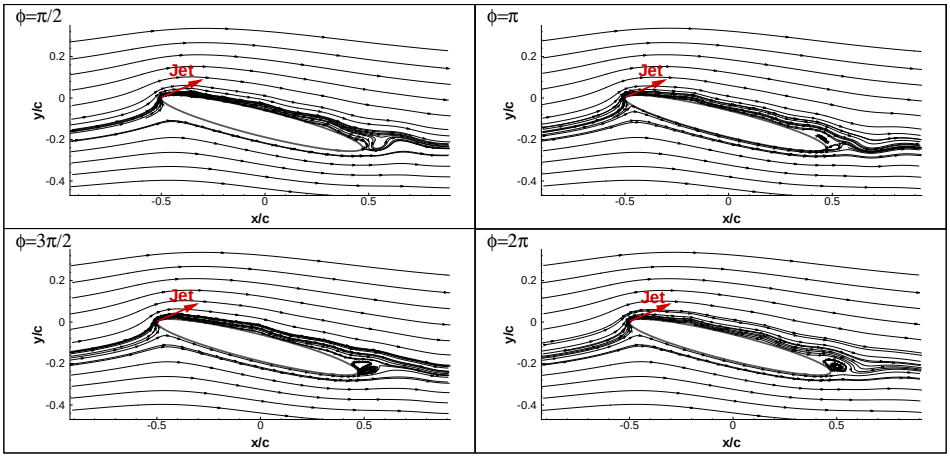

(c) Synthetic Jet

Figure 4.19: The instantaneous flowfields with presence of various jets

The instantaneous flowfields for with presence of various jets are shown at Figure 4.19. As seen from Figure 4.19(a), a flow separation exists and it starts at 0.9 chord. In Figure 4.19(b), a vortex is formed at leading edge and connects downstream. In Figure 4.19(c), a vortex is formed at the 0.9 chord and connects downstream.

To summarize, the steady jet causes a steady flow and, the pulsating and the synthetic jets cause periodic flow. The steady jet increases the lift more effectively and the synthetic jet reduces the drag more effectively. All jet profiles delay the flow separation.

4.5 Parametric Studies on the Synthetic Jet Parameters

Parametric studies are carried out to evaluate the influence of synthetic jets on the flow. Flow solutions are obtained at an angle of attack of 0 degrees, a freestream Mach number of 0.1 and Reynolds number of $1x10^6$. The jet velocity, the jet angle, the jet frequency, the jet location and the jet slot width are varied to observe their individual effects on the flow. The jet parameters of the baseline configuration are given in Table 4.1.

Table 4.1: The Jet Parameters of the Baseline Configuration

Jet Location	Jet Angle	Jet Slot Width	Jet Velocity	Jet Frequency
0.1	30	0.0047	1.5	1.2

Three jet locations are tested, $x/c = 0.1$, $x/c = 0.5$ and $x/c = 0.9$. Variation of the lift and the drag coefficients with the jet location are shown in Figure 4.20. As seen from the figure, the jet location at $x/c = 0.1$ reduces the drag coefficient by 3.66% and the jet location at $x/c = 0.9$ increases the lift by 217%.

To analyze effects of the jet angle, 15, 30 and 50 degrees are tested. Variation of the lift and the drag coefficients with the jet angle are presented in Figure 4.21. As seen from the figure, at jet location of $x/c = 0.1$ and the jet angle of 50 degrees decreases the drag by 8% and at jet location of $x/c = 0.9$ and the jet angle of 50 degrees increases the lift as much as 367% with a drag increase of 70%. Another observation is at jet location $x/c = 0.9$ and the jet angle of 30 degrees the lift is increased by 217% and the drag is stayed constant. It is observed that the jet angle effect on the flow is strongly related to the location of the jet.

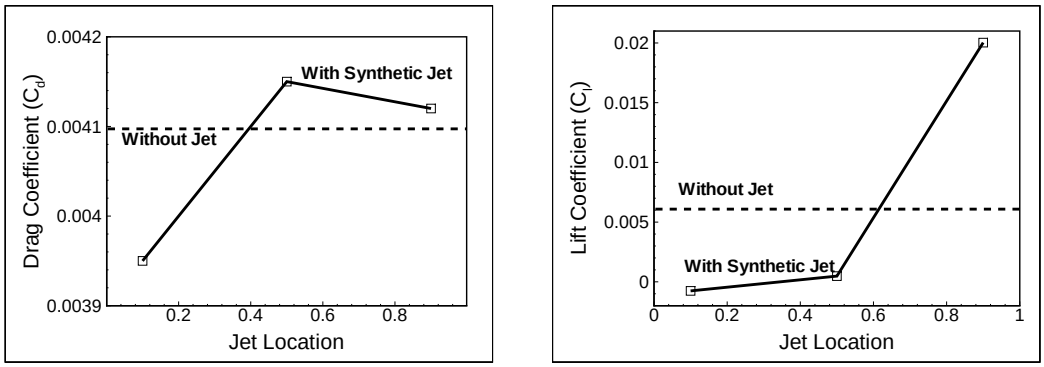

(a) (b)

Figure 4.20: Variation of the lift and the drag coefficients with the jet location

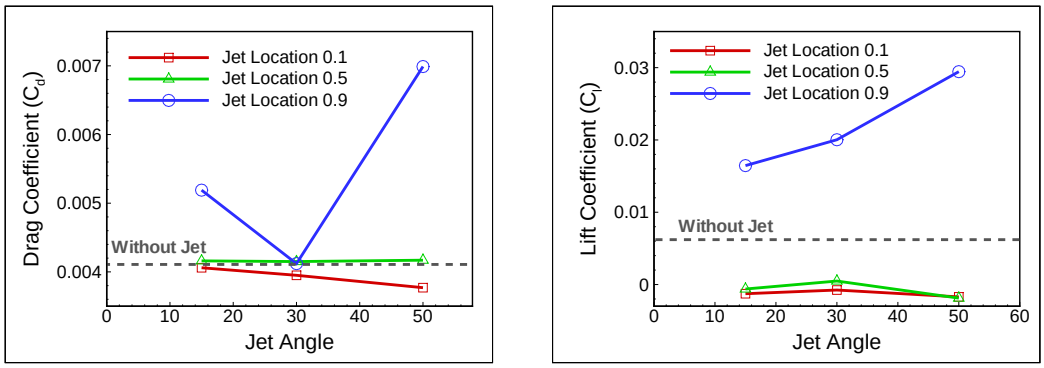

(a) (b)

Figure 4.21: Variation of the lift and the drag coefficients with the jet angle

The jet frequencies of 0.8, 1.2 and 3 are tested. Variation of the lift and the drag coefficients with the jet frequency are demonstrated in Figure 4.22. As can be observed, at jet locations of $x/c = 0.1$ and $x/c = 0.5$, the variation of jet frequency has almost no effect on the lift or the drag . At jet location of $x/c = 0.9$, the lift increases as the jet frequency increases. At jet location of $x/c = 0.9$ and the jet frequency of 3, the lift coefficient is increased by 349% with a 1% the drag decrease.

Three jet velocities (corresponding to Mach number) are tested; 0.1, 0.15 and 0.3. Variation of the lift and the drag coefficients with the jet velocity are illustrated in Figure 4.23. As seen from Figure 4.23(b), at all jet locations, the lift coefficient increases, as the jet velocity increases and the maximum the lift coefficient increase occurs at jet location $x/c = 0.9$ with

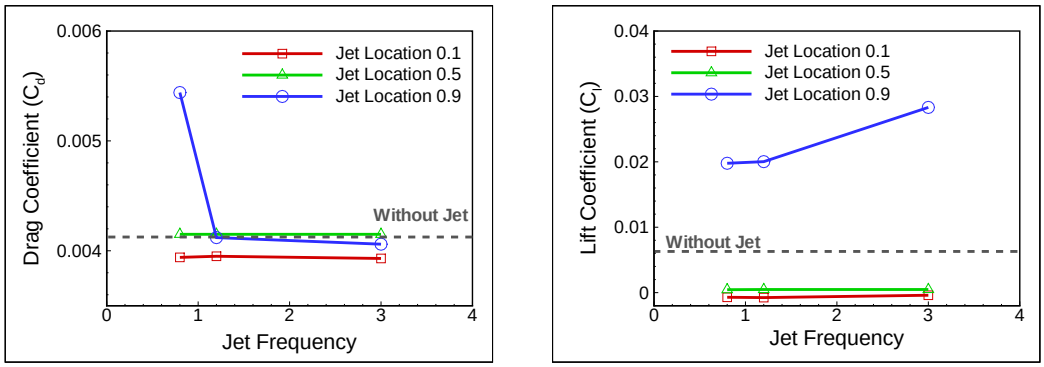

(a) (b)

Figure 4.22: Variation of the lift and the drag coefficients with the jet frequency

1285%.As observed from Figure 4.23(a), at jet locations $x/c = 0.1$ and $x/c = 0.5$, increasing the jet velocity decreases the drag coefficient and the maximum the drag reduction occurs at jet location 0.1 with 17.5%. At jet location $x/c = 0.9$, an increase of jet velocity results in first a decrease, then an increase in the drag . At jet location $x/c = 0.9$ with jet velocity 1.5, the drag stays constant, with the jet velocity 0.3, the drag increased by 81%. It is observed that increasing the jet velocity increases the jet momentum given to the flow and increasing the jet momentum increases the lift. However, increasing jet momentum may increase the drag also depending on the jet location.

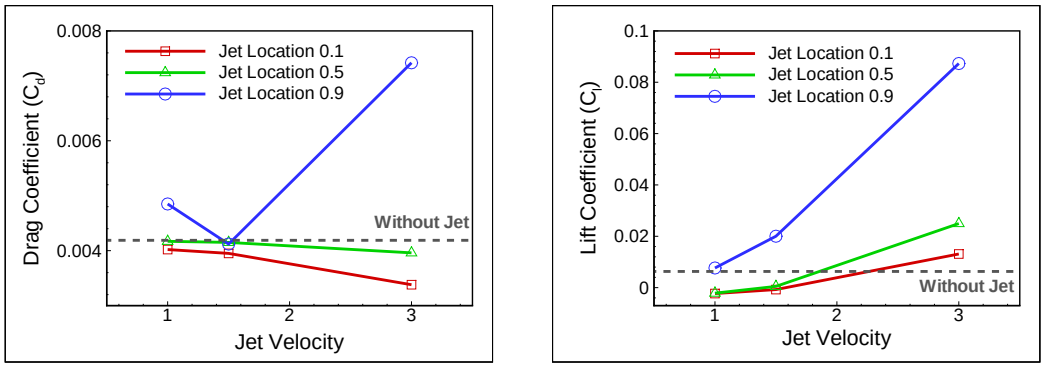

(a) (b)

Figure 4.23: Variation of the lift and the drag coefficient with the jet velocity

Three jet slot widths are tested; 0.00231, 0.0047 and 0.00707. Variation of the lift and the drag coefficients with the jet slot width are given in Figure 4.24. As seen from the figure, by

increasing the slot size both the lift enhancement and the drag reduction occur. The maximum the drag reduction of 5.6% is observed at the jet location of $x/c = 0.1$ and the jet slot width of 0.00707c. The maximum the lift enhancement of 300% is observed at the jet location of $x/c = 0.1$ and jet slot width of 0.00707c.

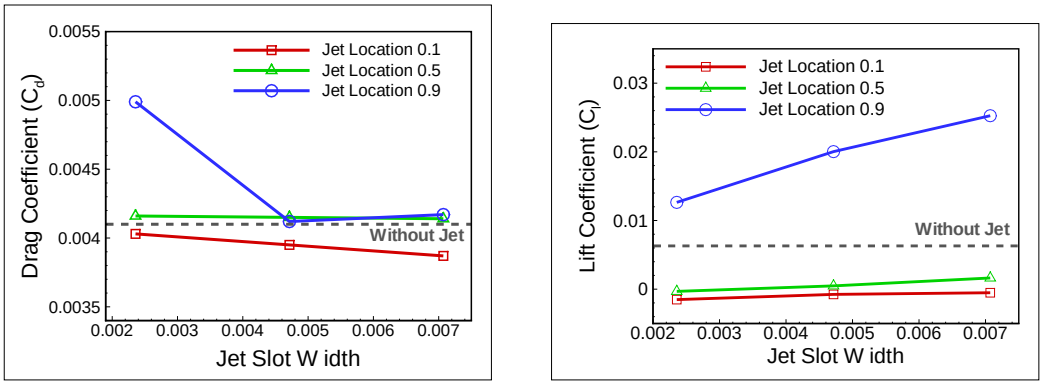

(a) (b)

Figure 4.24: Variation of The lift and the drag coefficients with the jet slot width

The flowfields for the cases with the minimum the drag and the maximum the lift are shown in Figure 4.25. As observed in Figure 4.25(c), implementation of the jet from 0.1 chord energizes the boundary layer and decreases the drag , whereas, in Figure 4.25(d), implementation of the jet from 0.9 chord delays the separation and increases the lift.

To summarize this subsection, the lift and the drag coefficient performance is strongly related to the location of the jet. The jet locations near leading edge are better for the drag reducing and the jet locations near trailing edge are better for the lift enhancement. The jet velocity and the jet slot width increase the lift and decrease the drag more effectively. The jet angle and the jet frequency effects are strongly related to jet location. The least effective parameter observed is the jet frequency.

4.6 Optimization of Synthetic Jet Parameters

The numerical optimization algorithm described in Chapter 3 is implemented for the synthetic jet parameters to minimize the drag coefficient of the elliptical profile. The optimization algorithm is based on the response surface of the objective function, which is the drag coefficient.

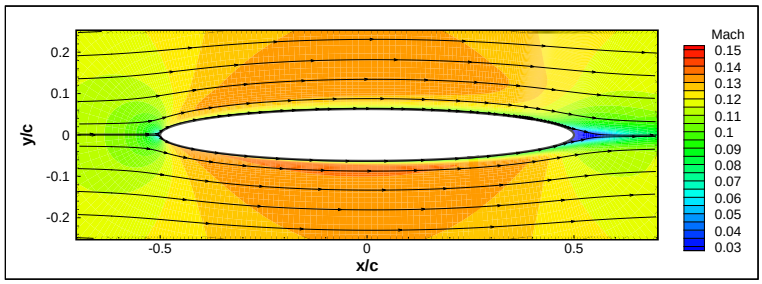

(a) Without Jet

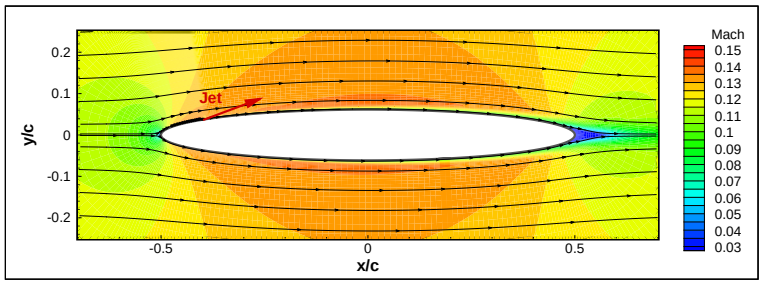

(b) With Jet - Baseline Configuration (Drag Change= -3.66%, Lift Change= -112%)

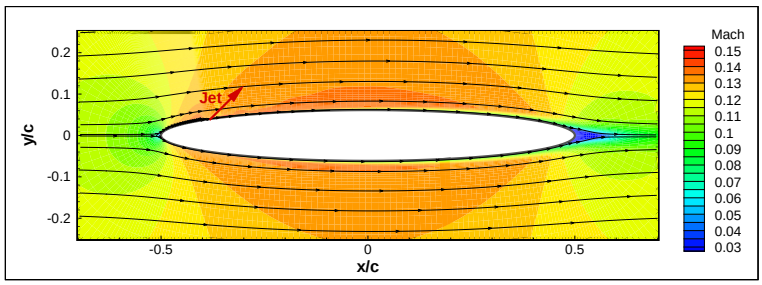

(c) With Jet - Minimum Drag (Drag Change= -17.56%, Lift Change= 108%)

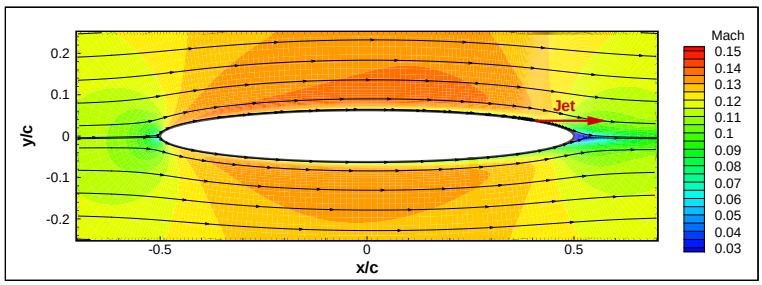

(d) With Jet - Maximum Lift (Drag Change= 81%, Lift Change= 1285%)

Figure 4.25: Average flowfields at α=0

The computational and experimental findings show that the drag coefficient is closely connected to synthetic jet and flow parameters, such as the jet velocity, the jet angle, the jet frequency, the jet location, the jet slot width, the angle of attack of the profile (α), etc. It is observed that, to minimize the drag coefficient an optimization of all above variables is needed. By keeping the jet power coefficient constant, the jet slot width becomes a function of the jet velocity, the jet angle and the jet frequency. The independent variables are reduced to four.

In this study, optimization variables are the jet slot width, the jet location, the jet velocity, the jet angle and the jet frequency. Two optimization studies are conducted with α=0 degrees and α=4 degrees.

Full Factorial Design of RSM gives the number of flow solutions as 3^4 for five independent variables. Limits of the optimization space for 4-variable RSM optimization is shown in Table 4.2.

Table 4.2: Limits of the Optimization Space for 4 Variable Full Factorial Design of Experiment RSM Optimization

	Jet Location	Jet Angle	Jet Velocity	Jet Frequency
Minimum	0.1	15	0.1	0.8
Mean	0.5	30	0.15	1.2
Maximum	0.9	50	0.3	3.

4.6.1 Optimization at α = 0 degrees

Optimization studies are performed for minimizing the drag coefficient. Flow solutions are obtained at an angle of attack of 0 degrees, a freestream Mach number of 0.1, Reynolds number of $1x10^6$ and a jet power coefficient of 0.0006.

The initial optimization study is conducted with Full Factorial Design of Experiment (DoE) and the ranges of parameters are specified in Table 4.2. In the initial optimization study the minimum the drag is computed as 0. The jet parameters are found as a jet location of x/c = 0.1, a jet frequency of 0.8, a jet velocity of 0.3 and a jet angle of 33^o. At the optimum point RANS calculates the drag coefficient as 0.00371 corresponding to a drag decrease of 9.5%. RSM residuals for initial optimization study are presented in Figure 4.26. Figure 4.26(a)

compares the flow solver results with the RSM surface results. As observed, some values are outside of the 95% confidence lines. Figure 4.26(b) shows the error between response surface and the flow solutions. As seen, the maximum error between RSM surface and the flow solver result is about 25%.

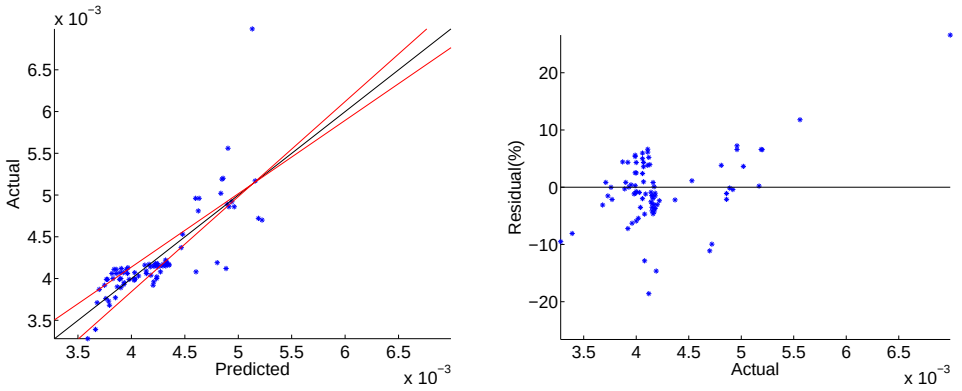

(a) (b)

Figure 4.26: RSM residuals at α=0 for first trial

To decrease the errors between the RSM surfaces and the flow solver, a second RSM set is performed. In the second RSM set a smaller range of variables and Box-Behnken DoE is employed. Limits of the optimization space for second optimization study are illustrated in Table 4.3.

Table 4.3: Limits of the Optimization Space for 4 Variable Box Behnken Design of Experiment RSM Optimization

	Jet Location	Jet Angle	Jet Velocity	Jet Frequency
Minimum	0.01	15	0.15	0.5
Mean	0.1	33	0.3	0.8
Maximum	0.2	50	0.4	1.2

In the second optimization study, with the jet location of 0.01 chord, a jet frequency of 0.5, jet velocity of 0.4 and a jet angle of 50^o the minimum the drag is computed as 0. At the optimum point RANS calculates the drag coefficient as 0.00277 corresponding to a drag decrease of 32.5%. The RSM residuals for second optimization study are shown in Figure 4.27. As seen, the error between the RSM surface and the flow solver result is nearly 11%. Figure 4.27(a)

compares the flow solver results with the RSM surface results. As observed, most of the values are within the of 95% confidence lines. The response surface plots are given in Figure 4.28. As seen, the most effective parameter is the jet location, then the jet velocity while the least effective parameter is the jet frequency.

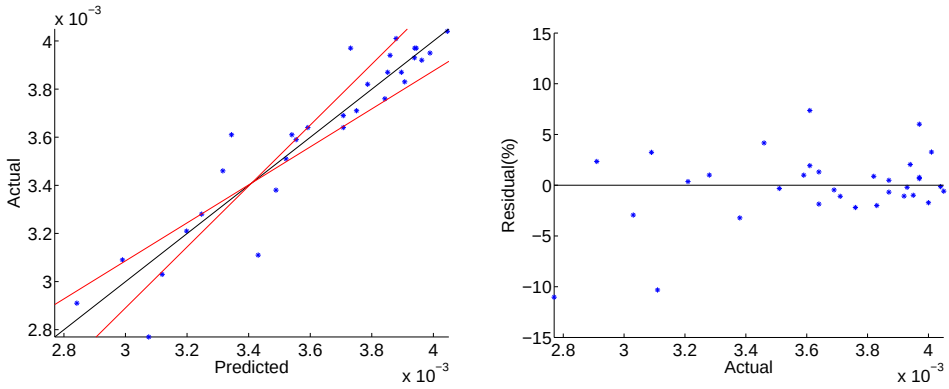

(a) (b)

Figure 4.27: RSM residuals at α=0 for second trial

At the baseline configuration of optimization, the lift coefficient is decreased about 112% and the drag coefficient is decreased about 3.66% . With optimization, the lift coefficient is increased about 34.5% and the drag coefficient is decreased about 32.5%. Figure 4.29 compares the average flowfields of without the jet, the synthetic jet applied with baseline configuration jet parameters and the synthetic jet applied with the optimum jet parameters. As seen from the figure, application of jet energized the boundary layer. However, the vortical structures at the trailing edge still exist.

4.6.2 Optimization at α = 4 degrees

Optimization studies are performed for minimizing the drag coefficient. Flow solutions are obtained at an angle of attack of 4 degrees, a freestream Mach number of 0.1, Reynolds number of 1x10^6 and a jet power coefficient of 0.0006.

The initial optimization study gives the minimum the drag as 0, the jet location as x/c = 0.1, the nondimensional jet frequency as 1.5, the jet velocity as 0.3 and the jet angle as 33^o. At the optimum point RANS calculates the drag coefficient as 0.00504, corresponding to a drag

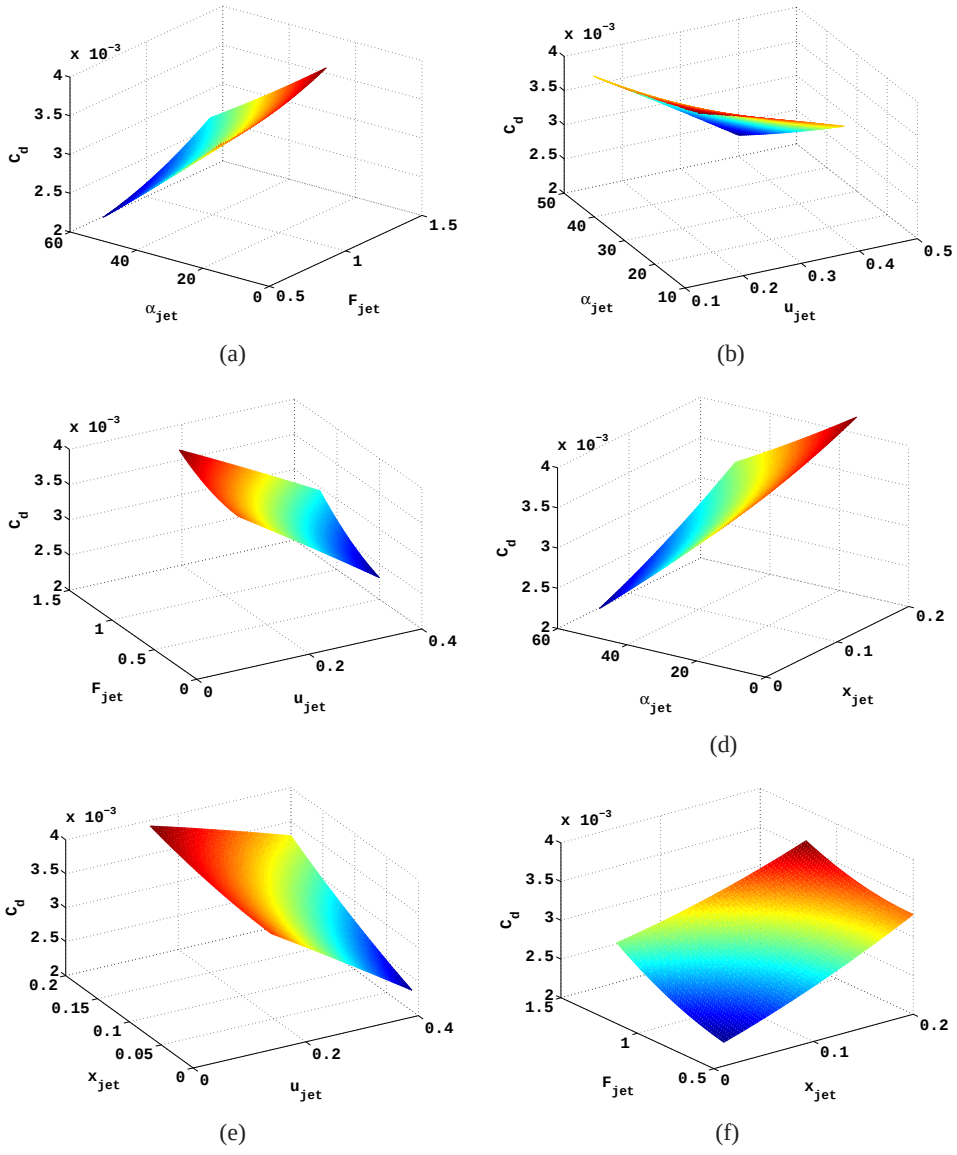

Figure 4.28: 3D plots of RSM at α=0 for second trial

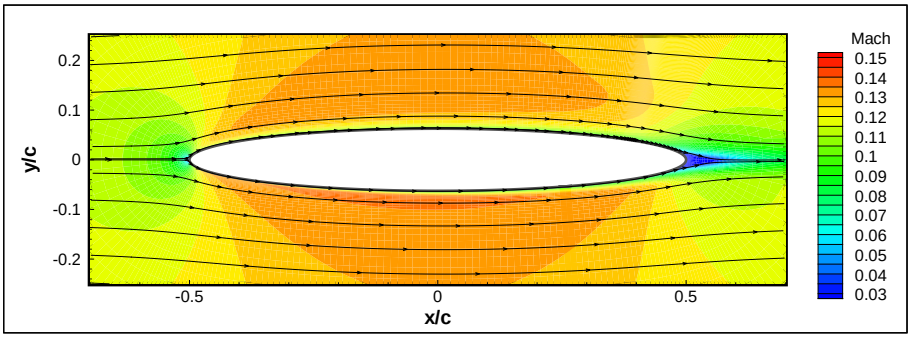

(a) Without Jet

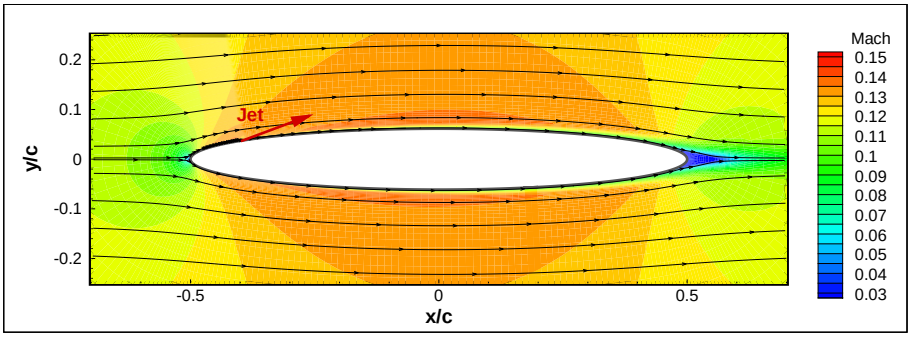

(b) With Jet - Baseline Configuration

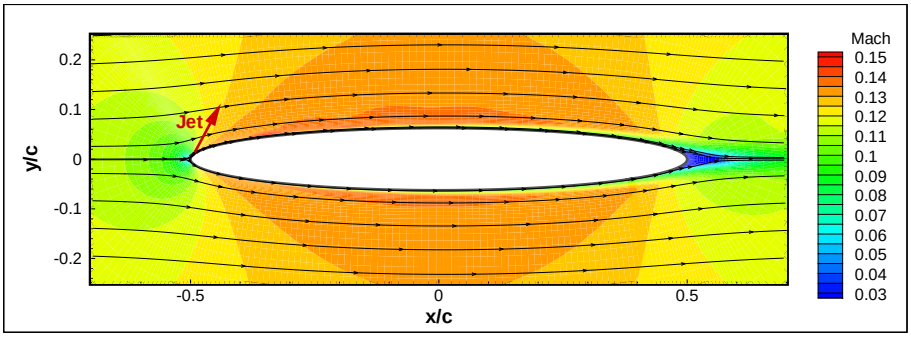

(c) With Jet - Minimum Drag Point

Figure 4.29: Average flowfields at α=0

reduction of 10%. RSM residuals for initial optimization study are given in Figure 4.30. As seen, the error between RSM surface and the flow solver result is less than 5%. Figure 4.30(a) compares the flow solver results with the RSM surface results. As observed, most values are within the 95% confidence lines. The response surface 3D plots are presented in Figure 4.31. As seen from the figure, the most effective parameter is the jet location followed by the jet velocity whereas the least effective parameter is jet frequency.

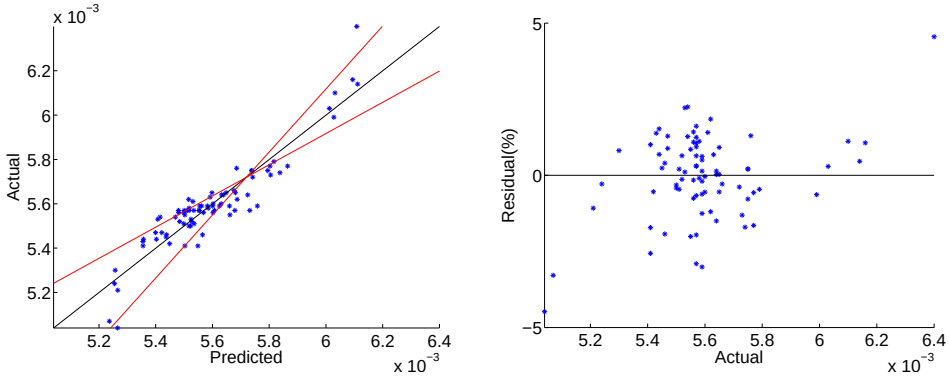

(a) (b)

Figure 4.30: RSM residuals at α=4 for first trial

To reduce the drag more the limits of DoE of RSM is modified. In the second RSM set a smaller range of variables and Box-Behnken DoE is employed. Limits of the optimization space for second optimization study are illustrated in Table 4.4.

Table 4.4: Limits of the Optimization Space for 4 Variable Box Behnken Design of Experiment RSM Optimization

	Jet Location	Jet Angle	Jet Velocity	Jet Frequency
Minimum	0.01	15	0.15	0.8
Mean	0.1	33	0.3	1.5
Maximum	0.2	50	0.4	3.

A second optimization study is performed using the limits in Table 4.4, since the drag reducing is too low. At the jet location of x/c = 0.01, with a nondimensional jet frequency of 0.8, jet velocity of 0.4 and a jet angle of 50^o, the minimum the drag is computed as 0. At the optimum point RANS calculates the drag coefficient as 0.00424 corresponding to a drag decrease of

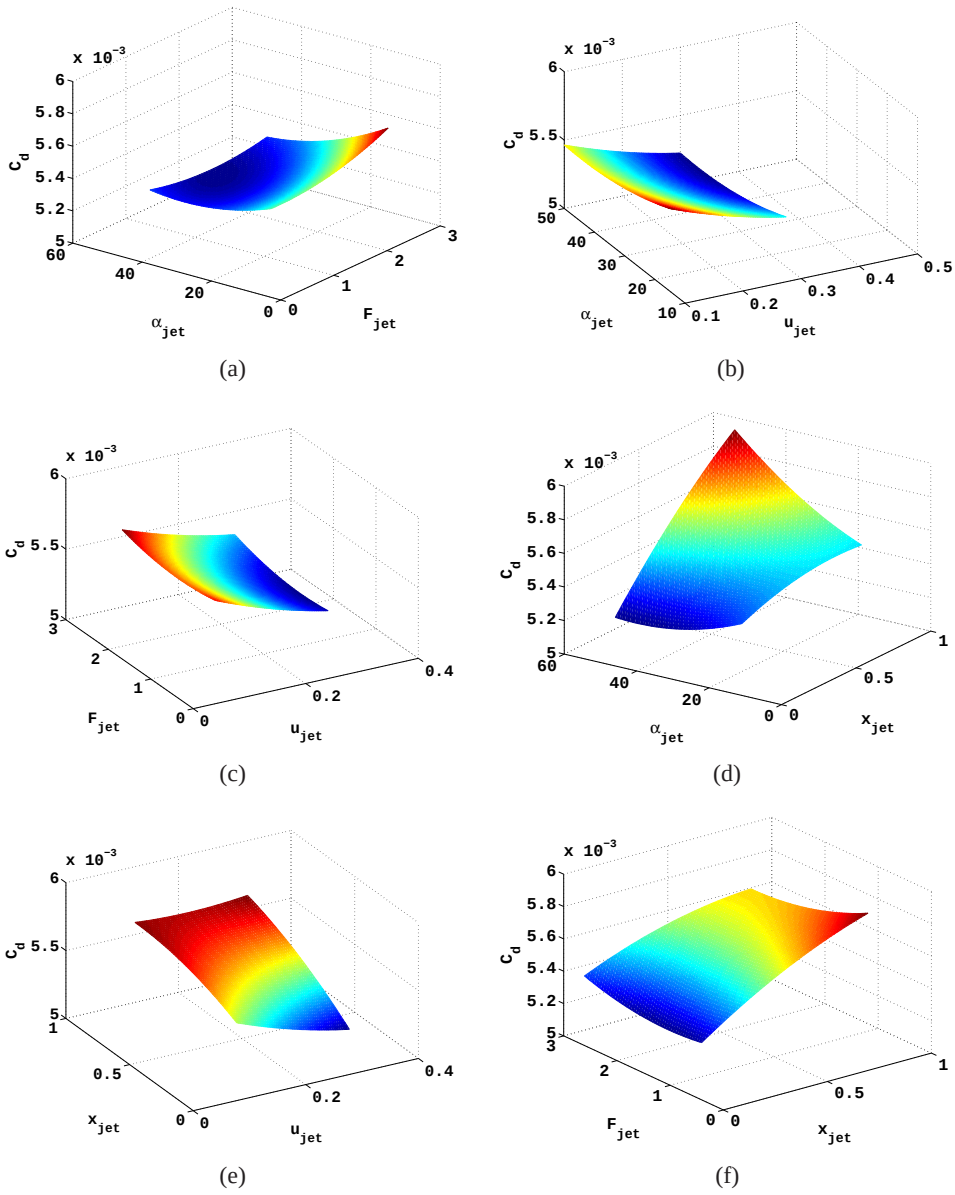

Figure 4.31: 3D plots of RSM at α=4 for first trial

24%. RSM residuals for second optimization study are given in Figure 4.32. As seen, the error between RSM surface and the flow solver result is less than 5%. Figure 4.32(a) compares the flow solver results with the RSM surface results. As observed, most values are within the 95% confidence lines. The response surface 3D plots are presented in Figure 4.33. As seen, the most effective parameter is the jet location followed by the jet velocity whereas the least effective parameter is jet frequency.

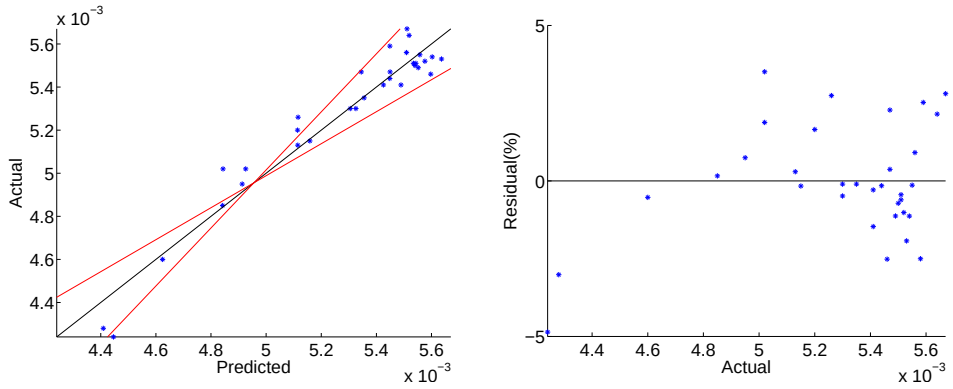

(a) (b)

Figure 4.32: RSM residuals at α=4 for second trial

At baseline configuration of optimization, the lift coefficient is not changed and the drag coefficient is decreased by 2%. At the optimum point the lift coefficient is increased by 2% and the drag coefficient is decreased by 24%. Figure 4.34 compares the average flowfields of without the jet, the synthetic jet applied with baseline configuration jet parameters and the synthetic jet applied with the optimum jet parameters. As seen, the boundary layer is energized as the jet is applied with optimum jet parameters are employed.

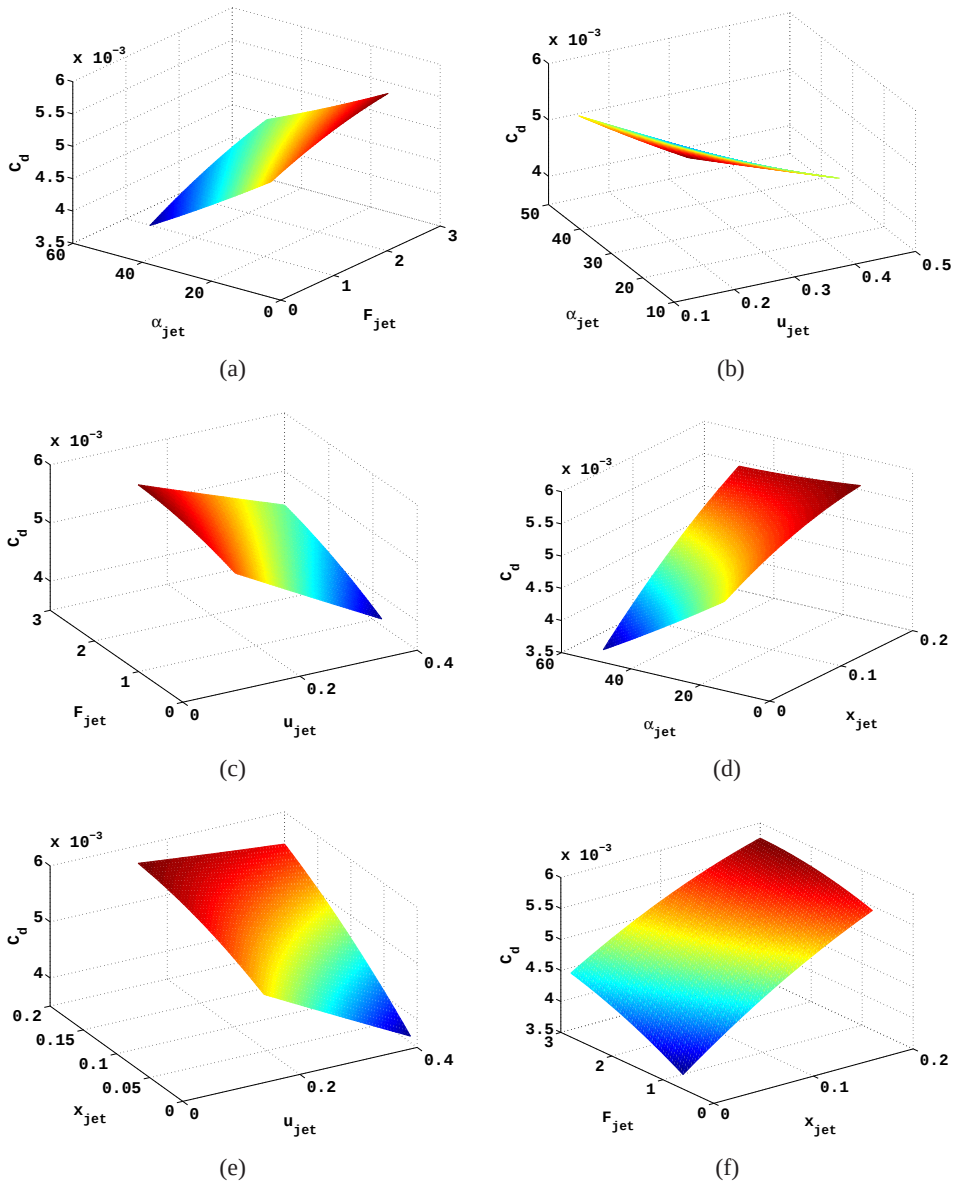

Figure 4.33: 3D plots of RSM at α=4 for second trial

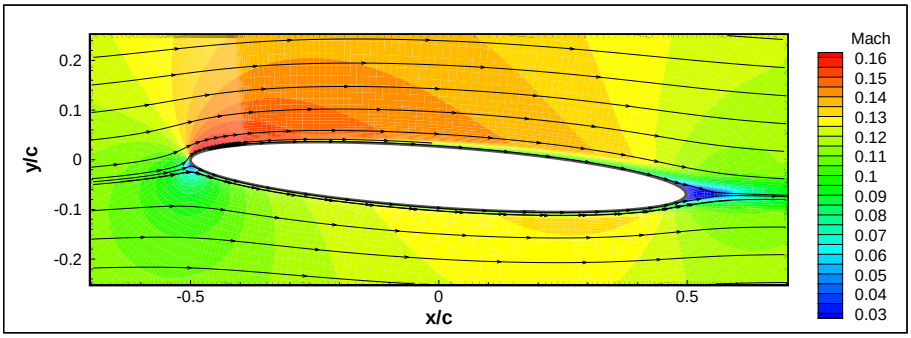

(a) Without Jet

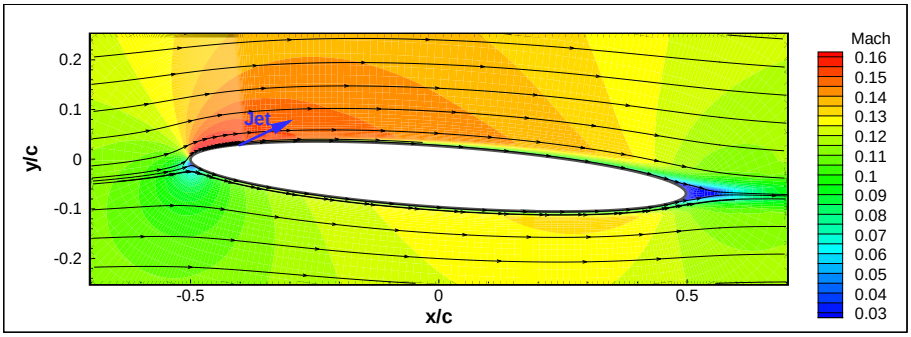

(b) With Jet - Baseline Configuration

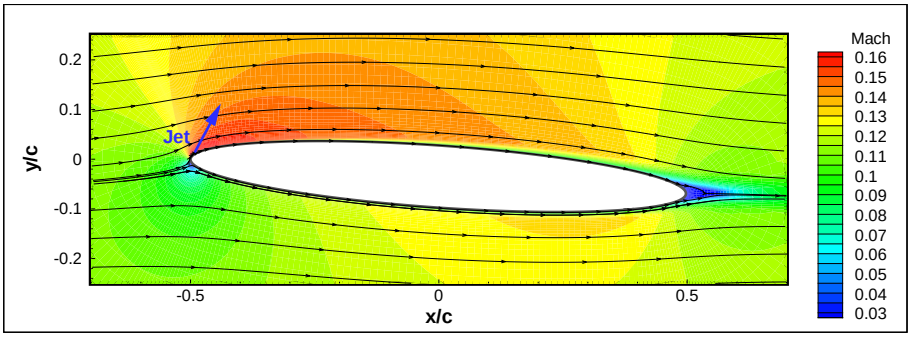

(c) With Jet - Minimum Drag Point

Figure 4.34: Average flowfields at α=4

CHAPTER 5

CONCLUSION

In the present study, active flow control studies with jets is performed successfully. Unsteady turbulent flows over a 12.5% thick elliptical profile are computed using a Navier Stokes solver, in a parallel computing environment, on structured grids. Validation studies are performed with and without the presence of the jet. The steady blowing, the pulsating and the synthetic jets are studied. The synthetic jet parameters are parametrized and optimized to minimize the drag.

In the validation studies without the presence of the jet, it is shown that the flow solutions agree well with the experimental study using transition location of $x/c = 0.1$. For steady blowing jets, it is observed that grid resolution at the jet location does not change the average C_p distribution significantly. The average C_p distributions of the three jet profiles, in general, agree well with the experimental data. The steady blowing jet applied at the leading edge causes lift enhancement and drag reduction at the same time. It is shown that sin^2 profile increases the C_l and decreases the C_d more effectively, and causes a steady flow. Applying the pulsating jet induces a periodic flow, where the frequencies of the C_l and the C_d are equal to the frequency of the pulsating jet. It is seen that the pulsating jet solutions are underestimating the seperation, causing overestimation of the average C_p. The Coanda effect is observed to cause a large increase in lift which is also increasing the drag. The solutions are shown to be underestimating the suction pressure at the trailing edge.

Preliminary studies of various jets; namely the steady blowing jet, the pulsating jet and the synthetic jet, are performed. The steady blowing jet causes steady flow, while other jets cause unsteady (periodic) flow. Application of the steady jet increases the lift the most and application of the synthetic jet decreases the drag the most. The least effective jet type is the

pulsating jet.

In the parametric studies of the synthetic jet following observations are achieved. As the jet velocity and the jet slot width increase, the lift increases and the drag decreases. The jet locations near leading edge are more effective for the drag reduction and the jet locations near trailing edge are more effective for the lift enhancement. The jet angle and the jet frequency effects are strongly related to the jet location. The least effective jet parameter is the jet frequency.

Finally, in the optimization of the synthetic jet parameters, it is observed that at $\alpha = 0$ degrees, for minimum drag, the jet should be applied at 0.01 chord with a nondimensional jet velocity of 0.4, with a jet angle of 50 degrees and a nondimensional jet frequency of 0.5. The drag is reduced by 32.5%, the lift is increased by 34.5%. For minimum drag at $\alpha = 4$ degrees, the jet should be applied at 0.01 chord with a nondimensional jet velocity of 0.4, with a jet angle of 50 degrees and a nondimensional jet frequency of 0.8. The drag is reduced by 24%, the lift is increased by 2%. The synthetic jet is, therefore, observed to be more effective at $\alpha = 0$ degrees.

As a future work, more sophisticated transition and turbulence models or LES, DNS can be used. To include 3D effects of turbulence, the problem can be modeled in 3D. The jet can be defined with different jet profiles or modeling can start from the diagphram of the synthetic jet. Oscillation of the jet velocity may be remodeled. More detailed parameterization of the jet parameters can be performed. The lift and the drag can be optimized together or the lift-to-drag ratio can be optimized. Different optimization techniques may be employed.

REFERENCES

[1] Glezer, A. and Amitay, M., "Synthetic Jets," *Annual Review of Fluid Mechanics*, Vol. 34, No. 1, 2002, pp. 503–529.

[2] Shrewsbury, G., "Numerical study of a research circulation control airfoil using Navier-Stokes methods," *Journal of Aircraft*, Vol. 26, No. 1, 1989, pp. 29–34.

[3] Gad-el Hak, M., "Modern developments in flow control," *Appl. Mech. Rev*, Vol. 49, No. 7, 1996, pp. 365–379.

[4] Kondor, S., Amitay, M., Parekh, D., Fung, P., and Glezer, A., "Active Flow Control Application on a Mini Ducted Fan UAV," *19th AIAA Applied Aerodynamics Conference*, 2001.

[5] Kondor, S., P. D. and Washburnt, A. E., "Investigations of Synthetic Jet Aerodynamic Control Modulation on a Full-scale UAV," *43rd AIAA Aerospace Sciences Meeting and Exhibit*, 2005.

[6] Lord, W., MacMartin, D., and Tillman, T., "Flow Control Opportunities in Gas Turbine Engines," *AIAA Paper*, Vol. 2234, 2000, pp. 19–22.

[7] Joslin, R., Gunzburger, M., Nicolaides, R., Erlebacher, G., and Hussaini, M., "A Self-contained, Automated Methodology for Optimal Flow Control Validated for Transition Delay," *AIAA Journal*, Vol. 35, No. 5, 1997, pp. 816–824.

[8] Choi, H., Moin, P., and Kim, J., "Active turbulence control for drag reduction in wall-bounded flows," *Journal of Fluid Mechanics Digital Archive*, Vol. 262, 2006, pp. 75–110.

[9] Liepmann, H. and Nosenchuck, D., "Active control of laminar-turbulent transition," *Journal of Fluid Mechanics Digital Archive*, Vol. 118, 2006, pp. 201–204.

[10] Jones, G., Viken, S., Washburn, A., Jenkins, L., and Cagle, C., "An Active Flow Circulation Controlled Flap Concept for General Aviation Aircraft Applications," *AIAA Paper*, Vol. 3157, No. 1, 2002.

[11] Sellers III, W., Jones, G., and Moore, M., "Flow Control Research at NASA Langley in Support of High-Lift Augmentation," *AIAA Paper*, Vol. 6006, 2002.

[12] Anders, S., Sellers, W., and Washburn, A., "Active Flow Control Activities at NASA Langley," *AIAA Paper*, Vol. 2623, No. 2, 2004.

[13] Hassan, A., Straub, F., and Domzalski, D., "Oscillating air jets for helicopter rotor aerodynamic control and BVI noise reduction," July 25 2000, US Patent 6,092,990.

[14] Vasilescu, R., *Helicopter Blade Tip Vortex Modifications in Hover Using Piezoelectrically Modulated Blowing*, Ph.D. thesis, Georgia Institute of Technology, 2004.

[15] Coanda, H., "Coanda Propelling Device," 1938, US Patent 2,108,652.

[16] Prandtl, L., "Uber Flussigkeitsbewegung bei sehr kleiner Reibung," *Verh. III. Intern. Math. Kongr., Heidelberg*, 1904, pp. 484–491.

[17] Lachmann, G., *Boundary Layer and Flow Control: Its Principles and Application*, Pergamon Press, 1961.

[18] Lachmann, G., *Boundary layer and flow control: Vol. 2*, Pergamon Press, 1961.

[19] Wells, W., "Means for Controlling Well Flow," 1936, US Patent 2,033,563.

[20] Barnwell, R., Bushnell, D., Nagamatsu, H., Bahi, L., and Ross, J., "Passive drag control of airfoils at transonic speeds," June 11 1985, US Patent 4,522,360.

[21] Hough, W., "Apparatus to control the water level in a swimming pool," Dec. 21 1976, US Patent 3,997,925.

[22] Hussaini, M. and Zang, T., *Spectral Methods in Fluid Dynamics*, Annual Reviews, 1986.

[23] Malik, M., Chuang, S., and Hussaini, M., "Accurate numerical solution of compressible, linear stability equations," *Zeitschrift für Angewandte Mathematik und Physik (ZAMP)*, Vol. 33, No. 2, 1982, pp. 189–201.

[24] Sun, M., P. S. and Chopra, I., "Aerodynamics force calculations of an elliptical circulation control airfoils," *Journal of Aircraft*, Vol. 23, No. 9, 1986, pp. 673–680.

[25] VanHorn, J., "Circulation Control Slots in Helicopter Yaw Control System," Aug. 14 1990, US Patent 4,948,068.

[26] Seifert, A., Darabi, A., and Wygnanski, I., "Delay of Airfoil Stall by Periodic Excitation," *Journal of Aircraft*, Vol. 33, No. 4, 1996, pp. 691–698.

[27] Naini, A., Greenblatt, D., Seifert, A., et al., "Active Control of Cylinder Flow with and without a Splitter Plate using Piezoelectric Actuators," *AIAA Paper 2002-3070*, 2002.

[28] Siegel, S., Cohen, K., and McLaughlin, T., "Feedback control of a circular cylinder wake in experiment and simulation," *AIAA Paper 2003-3569*, 2003.

[29] Jones, G. and Englar, R., "Advances in pneumatic-controlled high-lift systems through pulsed blowing," *21 st AIAA Applied Aerodynamics Conference*, 2003.

[30] Viswanath, P. and Madhavan, K., "Control of Trailing-Edge separation by tangential blowing inside bubble: a novel approach," *41st Aerospace Sciences Meeting and Exhibit,Reno, Nevada*, 2003.

[31] Donovan, J., Krai, L., and Cary, A., "Active Flow Control Applied to an airfoil," *AIAA Journal*, 1998, pp. 98–0210.

[32] Liu, Y., Sankar, L., Englar, R., and Ahuja, K., "Numerical Simulations of the Steady and Unsteady Aerodynamic Characteristics of a Circulation Control Wing Airfoil," *AIAA paper*, Vol. 704, 2001, pp. 8–11.

[33] Subhashini, S., Takhar, H., and Nath, G., "Non-uniform multiple slot injection (suction) or wall enthalpy into a compressible flow over a yawed circular cylinder," *International Journal of Thermal Sciences*, Vol. 42, No. 8, 2003, pp. 749–757.

[34] Viken, S., Vatsa, V., Rumsey, C., and Carpenter, M., "Flow Control Analysis on the Hump Model with RANS Tools," *41st Aerospace Sciences Meeting and Exhibit,Reno,Nevada*, 2003.

[35] Chakravarty, S. and Osher, S., "Numerical experiments with the Osher upwind scheme for the Euler equations," *AIAA Journal(ISSN 0001-1452)*, Vol. 21, 1983, pp. 1241–1248.

[36] Rai, M. and Chakravarty, S., "An implicit form for the Osher upwind scheme," *AIAA Journal*, Vol. 24, No. 5, 1986, pp. 735–743.

[37] Kaya, M., *Computation of Viscous Flows Over Flapping Airfoils and Parallel Optimization of Flapping Parameters*, Master's thesis, METU, 2003.

[38] Kaya, M., *Path Optimization of Flapping Airfoils Based on Unsteady Viscous Flow Solutions*, Ph.D. thesis, METU, 2008.

[39] Spalart, P. and Allmaras, S., "A one-equation turbulence model for aerodynamic flows," *30 th AIAA Aerospace Sciences Meeting and Exhibit*, 1992.

[40] Pope, S., *Turbulent Flows*, Cambridge University Press, 2000.

[41] Geist, A., Beguelin, A., Dongarra, J., Jiang, W., Manchek, R., and Sunderam, V., "PVM 3 Users Guide and Reference Manual," *Oak Ridge National Laboratory, Oak Ridge, Tennessee*, Vol. 37831, 1994.

[42] Tuncer, I., "Parallel Computation of Multi-Passage Cascade Flows on Partitioned Overset Grids," *XI Ulusal Mekanik Konferansi, Bolu, Turkey, 6-10 September*, 1999.

[43] Mavris, D., "An Introduction to RSM and its Role in the Paradigm Shift," Presentation, 2007.

[44] Mavris, D., "The Beginners Guide to Fitting Response Surfaces," Manual, 2007.

[45] Mavris, D., "Introduction to Response Surface Methods," Presentation, 2007.

[46] Mavris, D., "Introduction to Design of Experiments and Response Surface Methods," Presentation, 2007.

[47] Croarkin, C. and Tobias, P., "Engineering Statistics Handbook," *NIST & Sematech*, 2002.

[48] Sohn, M., Chung, H., and Tuncer, I., "Flow Separation Control of an Elliptical Wing by Pulsating Jet," *23 rd AIAA Applied Aerodynamics Conference*, 2005, pp. 1–13.